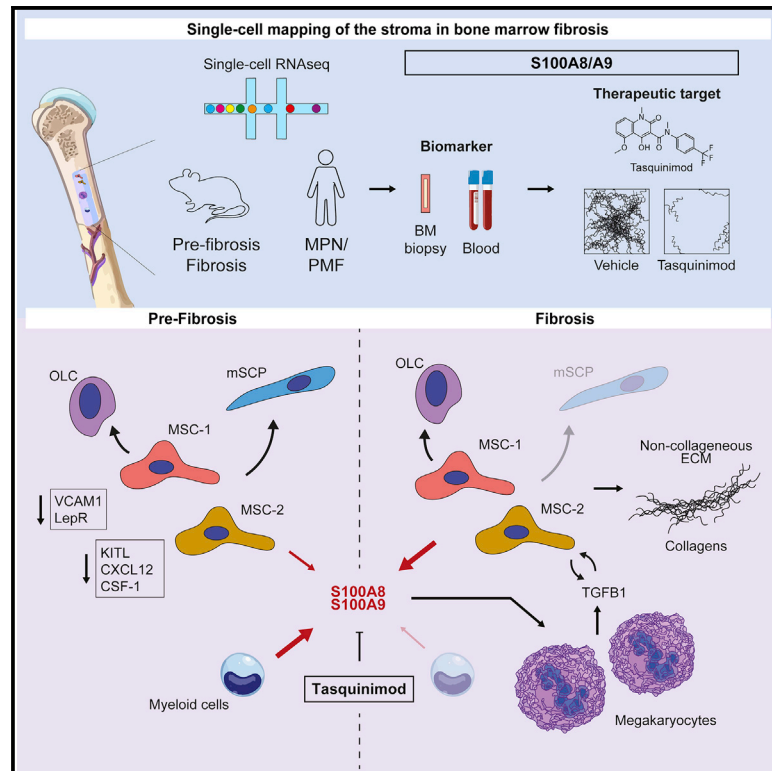


Heterogeneous bone-marrow stromal progenitors drive myelofibrosis via a druggable alarmin axis

Graphical Abstract



Authors

Nils B. Leimkühler, Hélène F.E. Gleitz, Li Ronghui, ..., Rafael Kramann, Ivan G. Costa, Rebekka K. Schneider

Correspondence

reschneider@ukaachen.de

In Brief

Leimkühler and colleagues demonstrate that mesenchymal stromal progenitor cells are fibrosis-driving cells in mice and patients, that inflammation in the bone-marrow stroma precedes TGF- β signaling-driven fibrosis, and that the alarmin heterocomplex S100A8/S100A9 holds promise as MPN progression marker and therapeutic target.

Highlights

- Mesenchymal progenitor cells are fibrosis-driving cells in the bone marrow
- Inflammation in the stroma characterizes pre-fibrosis and TGF- β signaling fibrosis
- Stromal S100A8/S100A9 marks disease progression in MPN patients
- Tasquinimod, inhibiting S100A8/S100A9 signaling, ameliorates the MPN phenotype



Article

Heterogeneous bone-marrow stromal progenitors drive myelofibrosis via a druggable alarmin axis

Nils B. Leimkühler,^{1,14} H el ene F.E. Gleitz,^{1,14} Li Ronghui,^{2,14} Inge A.M. Snoeren,¹ Stijn N.R. Fuchs,¹ James S. Nagai,² Bella Banjanin,¹ King H. Lam,³ Thomas Vogl,⁴ Christoph Kuppe,⁵ Ursula S.A. Stalmann,¹ Guntram B usche,⁶ Hans Kreipe,⁶ Ines G utgemann,⁷ Philippe Krebs,⁸ Yara Banz,⁸ Peter Boor,⁹ Evelyn Wing-Yin Tai,⁹ Tim H. Br ummendorf,¹⁰ Steffen Koschmieder,¹⁰ Martina Crysandt,¹⁰ Eric Bindels,¹ Rafael Kramann,^{5,13,15} Ivan G. Costa,^{2,15} and Rebekka K. Schneider^{1,11,12,15,16,*}

¹Department of Hematology, Erasmus Medical Center, Rotterdam 3015GD, the Netherlands

²Institute for Computational Genomics, Faculty of Medicine, RWTH Aachen University, Aachen 52074 Germany

³Department of Pathology, Erasmus Medical Center, Rotterdam 3015GD, the Netherlands

⁴Institute of Immunology, University of M unster, M unster 49148, Germany

⁵Division of Nephrology and Clinical Immunology, Faculty of Medicine, RWTH Aachen University, Aachen 52074, Germany

⁶Institute of Pathology, Hannover Medical School, Hannover 30625, Germany

⁷Institute of Pathology, University of Bonn, Bonn 53127, Germany

⁸Institute of Pathology, University of Bern, Bern 3012, Switzerland

⁹Institute of Pathology, Faculty of Medicine, RWTH Aachen University, Aachen 52074, Germany

¹⁰Department of Hematology, Oncology, Hemostaseology, and Stem Cell Transplantation, Faculty of Medicine, RWTH Aachen University, Aachen 52074, Germany

¹¹Department of Cell Biology, Institute for Biomedical Engineering, Faculty of Medicine, RWTH Aachen University, Pauwelsstrasse 30, 52074 Aachen, Germany

¹²Oncode Institute, Erasmus Medical Center, Rotterdam 3015GD, the Netherlands

¹³Institute of Experimental Medicine and Systems Biology, RWTH Aachen University, Aachen 52074, Germany

¹⁴These authors contributed equally

¹⁵These authors contributed equally

¹⁶Lead Contact

*Correspondence: reschneider@ukaachen.de

<https://doi.org/10.1016/j.stem.2020.11.004>

SUMMARY

Functional contributions of individual cellular components of the bone-marrow microenvironment to myelofibrosis (MF) in patients with myeloproliferative neoplasms (MPNs) are incompletely understood. We aimed to generate a comprehensive map of the stroma in MPNs/MFs on a single-cell level in murine models and patient samples. Our analysis revealed two distinct mesenchymal stromal cell (MSC) subsets as pro-fibrotic cells. MSCs were functionally reprogrammed in a stage-dependent manner with loss of their progenitor status and initiation of differentiation in the pre-fibrotic and acquisition of a pro-fibrotic and inflammatory phenotype in the fibrotic stage. The expression of the alarmin complex S100A8/S100A9 in MSC marked disease progression toward the fibrotic phase in murine models and in patient stroma and plasma. Tasquinimod, a small-molecule inhibiting S100A8/S100A9 signaling, significantly ameliorated the MPN phenotype and fibrosis in JAK2V617F-mutated murine models, highlighting that S100A8/S100A9 is an attractive therapeutic target in MPNs.

INTRODUCTION

Bone-marrow (BM) fibrosis is characterized by continuous replacement of blood-forming cells in the BM by excessive scar tissue. Primary myelofibrosis (PMF) is the prototypic example of progressive development of BM fibrosis. The hallmark feature of overt PMF is the excess deposition of extracellular matrix (ECM), which is accompanied by a progressive loss of hematopoiesis and splenomegaly due to extramedullary hematopoiesis. Although the molecular alterations in hematopoietic cells, which drive the development of myeloproliferative neo-

plasms (MPNs) have been largely defined (Vainchenker et al., 2011; Rampal et al., 2014), reactive cellular alterations in the non-hematopoietic compartment remain rather obscure. The BM morphology in patients with PMF suggests that there is a stepwise evolution from an initial pre-fibrotic phase to a fibrotic phase with marked reticulin/collagen fibrosis. However, the initial changes and sequential events underlying the pre-fibrotic phase of the disease are not well characterized (Barbui et al., 2018).

The plethora of stromal cells in a normal hematopoietic stem cell (HSC) niche (Baryawno et al., 2019; Tikhonova et al., 2019)



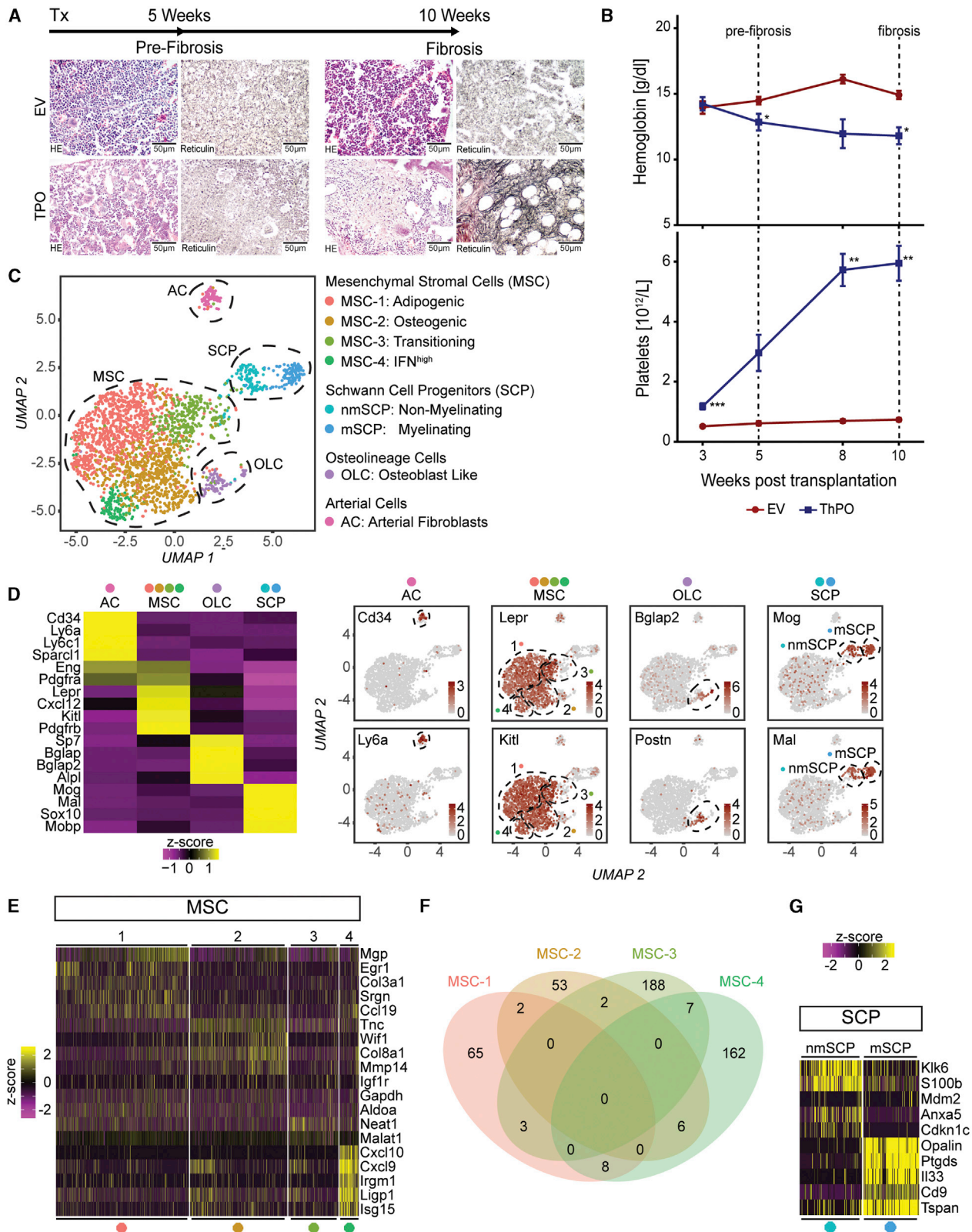


Figure 1. Identification of eight distinct non-hematopoietic cell populations

(A) HSPCs transduced with either thrombopoietin (ThPO) cDNA or control cDNA (EV) were transplanted (tx) at 0 weeks; n = 4 mice per time point and condition. Endpoint: 5 weeks (pre-fibrosis) and 10 weeks (fibrosis). Representative HE and reticulin staining. Scale bar, 50 μ m.

(legend continued on next page)

suggests that different stromal subtypes have distinct roles not only in normal hematopoiesis but also in BM fibrosis. In solid organ fibrosis, mesenchymal stromal cells (MSCs) are thought to be a major cellular source for fibrosis-driving cells (El Agha et al., 2017). These findings are mainly derived from genetic fate tracing experiments, which allow us to study the cell fate in response to a pathological stimulus. The well-accepted hypothesis in solid organ fibrosis is that fibrosis-inducing insults, e.g., pro-inflammatory and pro-fibrotic cytokines, affect MSCs and lead to a fate switch toward myofibroblasts, which, in turn, drive fibrosis by depositing ECM. In the BM, we and others demonstrated that MSCs contribute to fibrosis-driving $Gli1^+$ myofibroblasts (Decker et al., 2017; Schneider et al., 2017), but it remains an open question whether they are the only source of fibrosis-driving cells in the BM microenvironment or whether other cell types of the non-hematopoietic BM niche contribute to the fibrotic transformation. Here, we explored the cellular composition of the murine and human BM stroma by specifically profiling purified non-hematopoietic BM cells by scRNA sequencing (scRNA-seq) to identify fibrosis-driving cells and underlying mechanisms in MPNs using an unbiased approach.

RESULTS

Single-cell RNA-Seq of the BM niche captures eight major non-hematopoietic cell populations

To dissect the cellular composition and transcriptional changes of the murine BM stroma in the progression of BM fibrosis, we profiled non-hematopoietic BM cells by scRNA-seq in ThPO-induced BM fibrosis (Schneider et al., 2017). We analyzed (1) initial changes (pre-fibrotic stage) and (2) progression of BM fibrosis (fibrotic stage). Mice in the “pre-fibrotic” stage showed features of myeloproliferation and dysmorphic megakaryocytes but no reticulin fibers (reticulin grade 0, Figure 1A). In the fibrotic stage, mice developed severe BM fibrosis (Figure 1A). The hemoglobin (Hb) levels significantly decreased in ThPO-overexpressing mice as a surrogate marker for progression of BM fibrosis (Figure 1B). Mice exhibited significant thrombocytosis, when transplanted with ThPO-overexpressing HSPCs (Figure 1B), recapitulating the peripheral myeloproliferative phenotype observed in patients. We purified stromal cells from murine BMs at the pre-fibrotic time point and also the late, fibrotic time point (Table S1).

Unsupervised clustering of only non-hematopoietic niche cells identified eight distinct subclusters, which were grouped into four major cell populations (Figure 1C). The most dominant cluster was characterized by high expression of Leptin receptor (*Lepr*), platelet-derived growth factor receptor α (*Pdgfra*), and vascular cellular adhesion molecule 1 (*Vcam1*) as well as high levels of hematopoiesis supporting factors like *Cxcl12*, Kit ligand

(*Kitl*), and angiopoietin (*Angpt1*), and was thus classified as MSCs (Figure 1D). The other clusters were identified as osteolineage cells (OLCs; *Bglap*, *Sp7*, *Alpl*), arterial cells/adventitial fibroblasts (ACs; *Cd34*, *Ly6a*, *Ly6c1*), and Schwann cell progenitors (SCPs; *Mog*, *Mal*, *Plp1*; Figures 1C and 1D).

Within the $Lepr^+$ fraction, four subpopulations of MSCs were identified, in line with recent reports (Baryawno et al., 2019; Tikhonova et al., 2019). The dominant cluster exhibited an adipogenic signature with high levels of Matrix Gla protein (*Mgp*) and Adiponectin (*Adipoq*, Figure S1B) as well as a strong expression of hematopoiesis supporting genes (e.g., *Cxcl12*, *Kitl*; referred to as MSC-1; adipogenic MSCs; Figures 1C and 1E). The second MSC subcluster was characterized by an osteogenic expression pattern (*Spp1*, *Wif1*, *Ibsp*, *Sp7*, *Bglap*; MSC-2; osteogenic MSCs; Figures 1C and 1E). In the third cluster (MSC-3), high transcript levels of genes involved in chromatin remodeling and RNA processing indicated that these cells are in a transition state between different functional states of MSCs (Wu et al., 2017; Figure S1D). Gene set enrichment analysis of cluster 4 (MSC-4) revealed that these cells are strongly primed by a response to type 1 and type 2 interferons (Figure 1E; Figure S1D). Comparison of the identified MSC marker genes between the different subpopulations and their respective aggregate gene expression analysis confirmed four distinct MSC populations (Figure 1F; Figure S1E).

We further identified two distinct populations characterized by a Schwann cell precursor (SCP) signature (Figure 1G) indicated by *Cdh19* expression (SCPs; Figure S1C): non-myelinating SCPs (nmSCPs) and myelinating SCPs (mSCPs; Figure 1G).

Increased frequency of MSCs and glial cells in BM fibrosis

All identified cell clusters were present in fibrosis and control, but significant changes in cellular compositions of particular clusters were detected (Figure 2A). In fibrosis, MSC-1 and OLCs significantly increased in their frequency, while MSC-3 and -4 significantly decreased (Figure 2A, right panel). Interestingly, mSCPs depicted the most drastic cell expansion in fibrosis. SCPs are cells with high regenerative potential and their contribution to HSC maintenance was recently demonstrated (Yamazaki et al., 2011). Potentially, mSCPs expand in response to the myeloproliferative stimulus in MPNs as a regenerative mechanism.

Two distinct subpopulations of MSC are functionally reprogrammed in BM fibrosis to ECM-secreting cells

ECM production is considered the key feature of fibrosis (Friedman et al., 2013). We therefore asked which cells show the most significant expression of ECM specific genes in order to identify cells that drive BM fibrosis, so called myofibroblasts. We dissected the expression of gene sets defined for matrix-associated genes among the different clusters (Naba et al., 2016). In particular, MSCs, OLCs, and ACs showed the highest expression of ECM in fibrosis (Figure 2B) (Naba et al., 2016).

(B) Hemoglobin (Hb) and platelet counts over time (mean \pm SEM). Two-way-ANOVA with post hoc pairwise t test was used.

(C) UMAP of the non-hematopoietic BM niche identified by unsupervised clustering (n = 2,294 cells).

(D) Average gene expression of top marker genes within major cell populations (left panel). Feature plot of top markers in UMAP (right panel) is shown. Wilcoxon rank-sum test, $p < 0.01$. A full list of marker genes and corresponding GO terms is in Table S2.

(E) Heatmap of different MSC marker genes. Wilcoxon rank-sum test, $p < 0.01$.

(F) Venn diagram of the four identified MSC populations. Shared markers are highlighted in intersections.

(G) Heatmap SCP marker genes. Wilcoxon rank-sum test, $p < 0.01$.

See also Figure S1 and Tables S1 and S2.

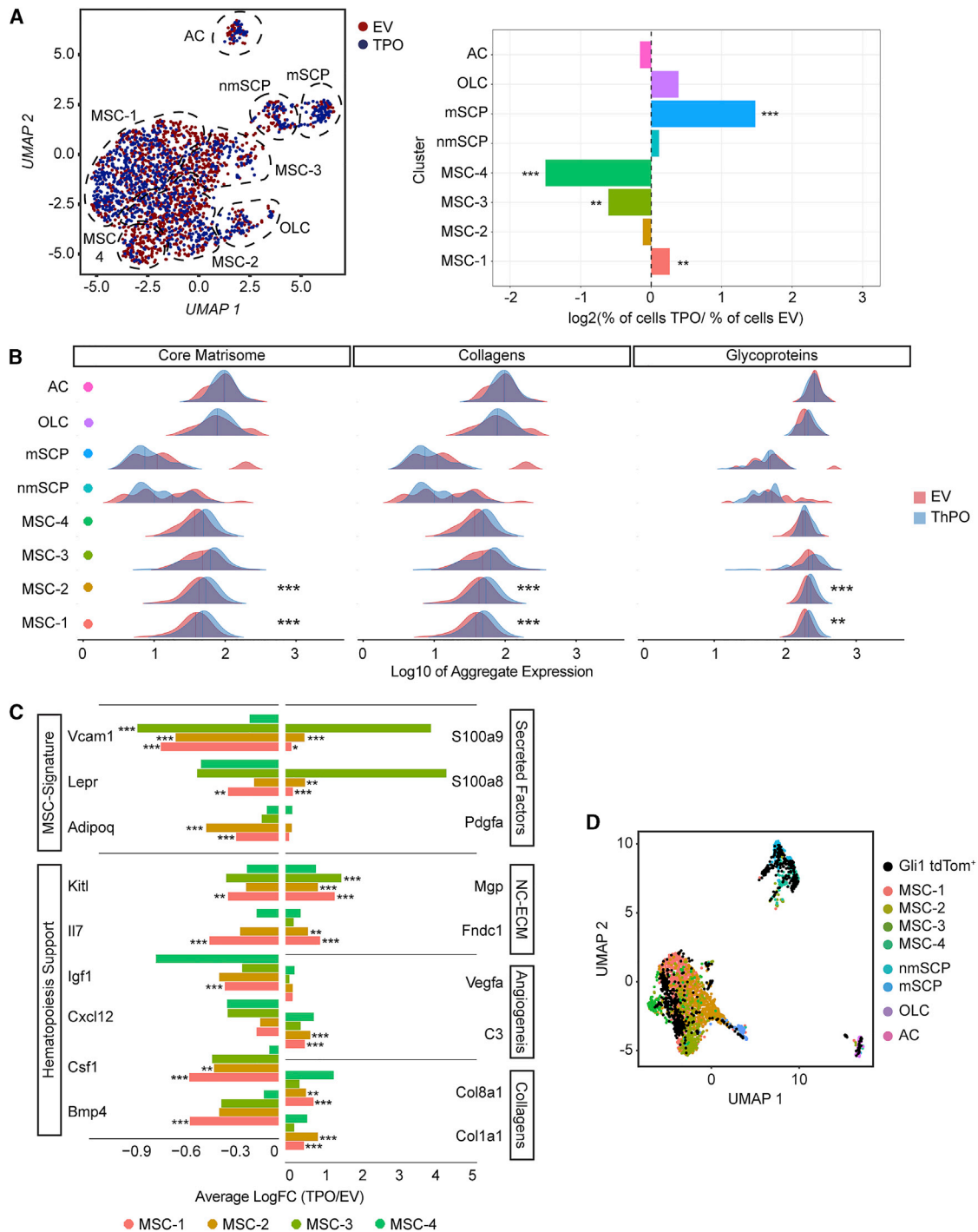


Figure 2. Mesenchymal stromal cells -1 and -2 represent the fibrosis-driving cells in ThPO-induced bone-marrow fibrosis

(A) Left panel: UMAP of non-hematopoietic cells from mice transplanted with thrombopoietin (ThPO; blue) or empty vector (EV; red; 5 and 10 weeks). Right panel: bar plot of cells per cluster (ThPO versus EV). Normalization to overall number of input per condition is shown. Fisher's exact test with Bonferroni correction was used.

(B) Ridgeline plot comparing expression of NABA matrisome-associated gene sets (ThPO; blue versus control EV; red) condition. Competitive gene set enrichment analysis was used.

(C) Normalized differential gene expression (ThPO versus EV) of indicated genes in MSCs (Wilcoxon rank-sum test, two tailed).

(D) Overlap of the non-hematopoietic compartment and FACS Gli1⁺ cells in UMAP space.

See also [Figure S2](#) and [Tables S3](#) and [S4](#).

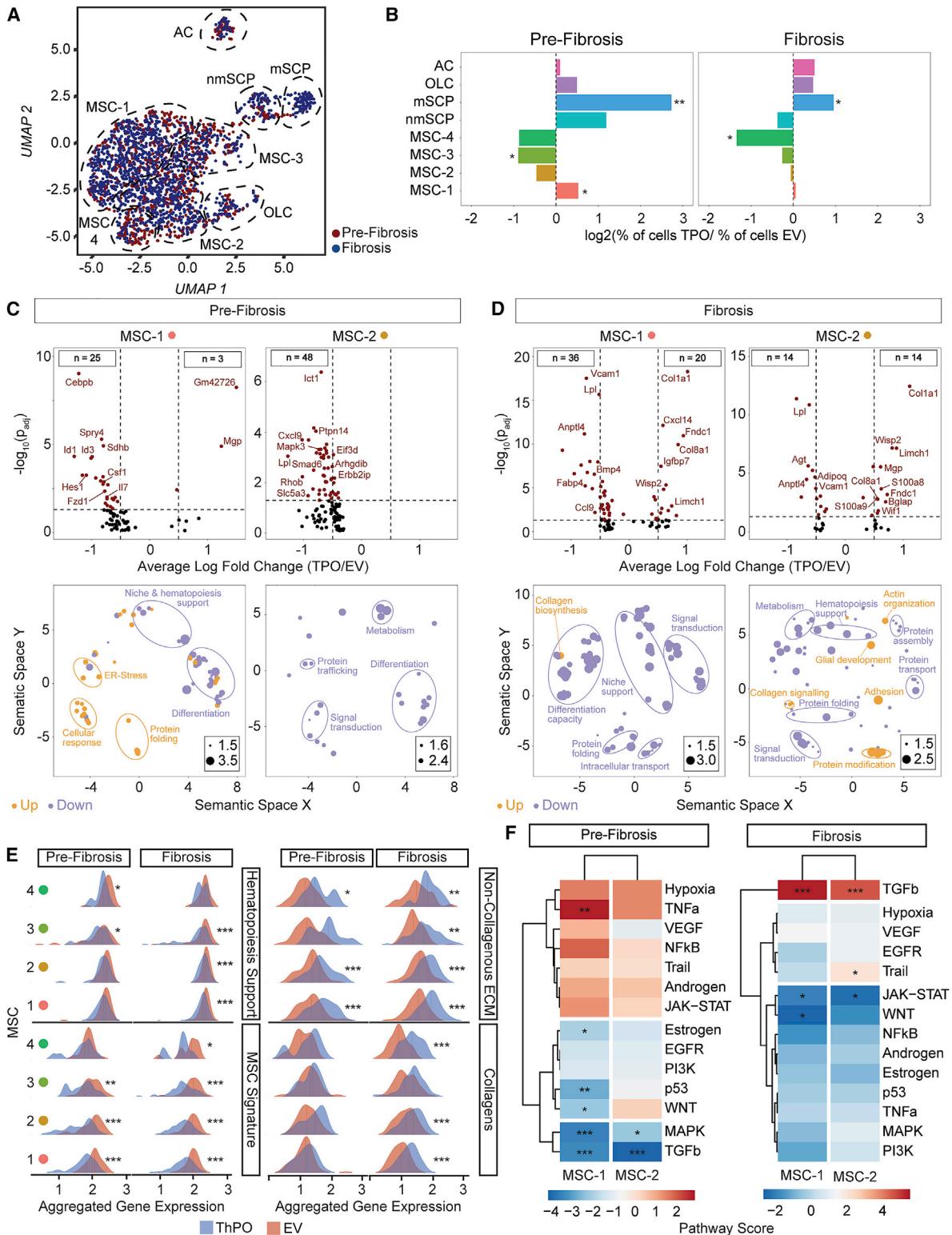


Figure 3. Mesenchymal stromal cells -1 and -2 are reprogrammed in pre-fibrosis and acquire a pro-fibrotic phenotype in fibrosis

(A) UMAP of non-hematopoietic single cells in pre-fibrosis (5 weeks; red) and fibrosis (10 weeks; blue).

(B) Bar plot of cells per cluster in ThPO versus EV after normalization to input per condition. Fisher's exact test with Bonferroni correction was used.

(legend continued on next page)

Importantly, only MSC-1 and MSC-2 showed a significant upregulation of ECM proteins in BM fibrosis, indicating that these two populations are the cellular drivers of the fibrotic progression and acquire myofibroblast characteristics. The most significantly downregulated genes in MSCs were grouped into (1) downregulated genes and (2) upregulated genes with onset of the MPN phenotype (Figures 2C; Figure S2A). The downregulated genes comprised (1) MSC markers (*Vcam*, *Lepr*, *Adipoq*) and (2) hematopoiesis support (*Kitl*, *Il7*, *Igf1*, *Cxcl12*, *Csf1*, *Bmp4*). The upregulated genes were defined through four major biological processes: (1) secreted factors (*S100a8*, *S100a9*, *Pdgfa*), (2) osteogenesis (*Mgp*, *Fndc1*), (3) neoangiogenesis (*Vegfa*, *C3*), and (4) ECM synthesis (*Col8a1*, *Col1a1*).

As MSC-1 and -2 by gene expression seemed to be the most primitive MSCs and fibrosis-driving cells, we wondered whether they can be discriminated by surface markers from MSC-3 and -4. We isolated MSC-1 and -2 (*Pdgfra/b*⁺, *Vcam1*⁺, *CD63*⁺, *Lamp1*⁺) and MSC-3 and -4 (*Pdgfra/b*⁺, *Vcam1*⁺, *CD63*⁻, and *Lamp1*⁻) by fluorescence-activated cell sorting (FACS) for subsequent functional testing (Figures S2B and S2C). MSC-1 and -2 formed significantly more colony-forming units fibroblast (CFU-F) and had a higher cell-division rate, as compared to MSC-3 and MSC-4, highlighting their progenitor status (Figures S2D and S2E). Importantly, they were also more sensitive to profibrotic transforming growth factor (TGF)- β stimulation *in vitro* as indicated by higher upregulation of *Col1a1* and *Acta2* mRNA as compared to MSC-3 and -4 (Figure S2F). In the context of differentiation into fibrosis-driving α -SMA and *Col1a1* expressing cells, MSC-1 and -2 strikingly downregulated *Cxcl12*, supporting our finding that these cells lose their hematopoiesis support during myofibroblast differentiation. Quantification of the frequency of MSC-1 and -2 in ThPO-induced BM fibrosis further supported the finding that these progenitor subsets are expanded in fibrosis while MSC-3 and -4 were decreased in their frequency (Figure S2G), in line with the data on the single-cell level (cf. Figure 2A).

Gli1⁺ cells comprise fibrosis-driving MSC-1 and -2 and Schwann cell precursors

Surprisingly, SCPs and mSCPs, which most drastically expanded in fibrosis, only revealed minor transcriptomic changes in ThPO versus EV conditions. However, mSCPs were characterized by high and specific expression of Interleukin-33 (*Il-33*) and Prostaglandin D2 synthase (*Ptgds*), implied to play central roles in solid organ fibrosis (Ito et al., 2012; Kotsiou et al., 2018) (Figure S2H). Previously, we demonstrated that Gli1⁺ cells are fibrosis-driving cells in the BM. To reliably label Gli1⁺ cellular subsets of the BM niche, we used Gli1CreER;tdTomato reporter mice (Schneider et al., 2017) for FACS-based purification for scRNA-seq. We integrated the data with stromal cells derived from the negative selection approach (Figure 2D; cf. Figure 1C; Table S1). Interestingly, Gli1⁺ cells are mostly MSCs, comparable to LepR⁺ cells but particularly annotated

as MSC-1 (41%) and -2 (19%), the fibrosis-driving cells, explaining our previous finding that genetic ablation of these cells ameliorates BM fibrosis (Schneider et al., 2017). Gli1⁺ cells are also represented in the mSCP cluster (26%), in line with MSC being derived from neural crest and comparable to the Nestin⁺ population, which also contains SCPs (Isern et al., 2014).

MSCs are functionally reprogrammed in pre-fibrosis and acquire a secretory, fibrotic, and osteogenic phenotype in manifest fibrosis

Next, we asked which cellular composition and transcriptional changes are characteristic for niche cells in the stepwise evolution of BM fibrosis (Figures 3A and 3B). Fibrosis-inducing MSC-1, both SCP populations and OLCs expanded in the pre-fibrotic phase while all other MSC populations decreased. In manifest fibrosis, IL33-expressing mSCPs, OLCs, and ACs expanded (cf. Figure 1A). To understand overall transcriptional changes across the different populations in pre-fibrosis and fibrosis, we performed differential expression analysis. All MSC clusters (MSC-1 to -4) showed mostly downregulated genes in pre-fibrosis compared to control (Figure 3C; Figure S3A) while none of the other niche cell types showed transcriptional changes, neither in pre-fibrosis nor in fibrosis (Figures S3B and S3C).

In pre-fibrosis, fibrosis-driving MSC-1 revealed ER stress and a significant downregulation of genes compared to the control condition (Figure 3C). The downregulated genes in MSC-1 and -2 indicated significant “transcriptional reprogramming” of these populations with loss of their core cellular characteristics: (1) loss of niche and hematopoiesis support as well as neurotrophic (e.g., *Fzd1*, *Cebpb*) and vascular signaling (e.g., *Foxc2*, *Hes1*), (2) loss of MSC multipotent progenitor status (e.g., *Arntl*, *Arhgdib*, *Ddr1*, *Lamb1*), (3) decreased cellular function (e.g., *Mapk3*, *Msn*), and (4) metabolic inactivation (e.g., *Cat*, *Tblxr1*, *Dgat1*, *Pank2*). In manifest fibrosis, MSC-1 and -2 upregulated numerous genes, which confirmed the functional reprogramming with loss of niche-supportive characteristics and loss of multipotent progenitor status (Figure 3D). MSC-1 was characterized by marker genes for myofibroblasts (e.g., upregulation of *Igfbp7*, *Limch-1*, *Wisp-2*) and extensive ECM and collagen synthesis (mainly *Col1a1*, *Col8a1*). Changes in MSC-2 indicated that these cells differentiate into (1) myofibroblasts (e.g., upregulation of *Limch1*, *Gas7*, *Acta1*), (2) osteoblasts (e.g., upregulation of *Bglap*), and (3) also glial cells (e.g., upregulation of *S100a8*, *S100a9*), potentially also compensating for the neuropathy and Schwann cell death in MPNs.

To validate our hypothesis that MSCs are reprogrammed in early stages of fibrosis and are fibrosis-driving myofibroblasts, which do not support normal hematopoiesis in manifest fibrosis, we defined gene sets based on the literature (Table S4) to interrogate “hematopoiesis support,” “MSC progenitor phenotype,” “non-collagenous ECM,” and “collagenous ECM” and plotted the dynamics of these gene sets in pre-fibrosis and fibrosis

(C and D) Volcano plot (ThPO versus EV) of differentially expressed genes (Wilcoxon rank-sum test, two tailed; calculated per cluster individually; top panel). Associated gene ontology terms (biological processes; BP; Fisher exact test; single tailed) plotted semantically (bottom panel) in (C) pre-fibrosis and (D) fibrosis. (For a complete list of GO-terms and corresponding genes, see Tables S2 and S3.)

(E) Ridgeline plot of functional gene sets (as indicated) in ThPO (blue) versus EV (red). Competitive gene set enrichment analysis.

(F) PROGENy analysis of MSC-1 and MSC-2 in pre-fibrosis and fibrosis. Sampling based permutation (10,000 permutations). Pathway activity scores as Z scores. See also Figure S3 and Tables S3 and S4.

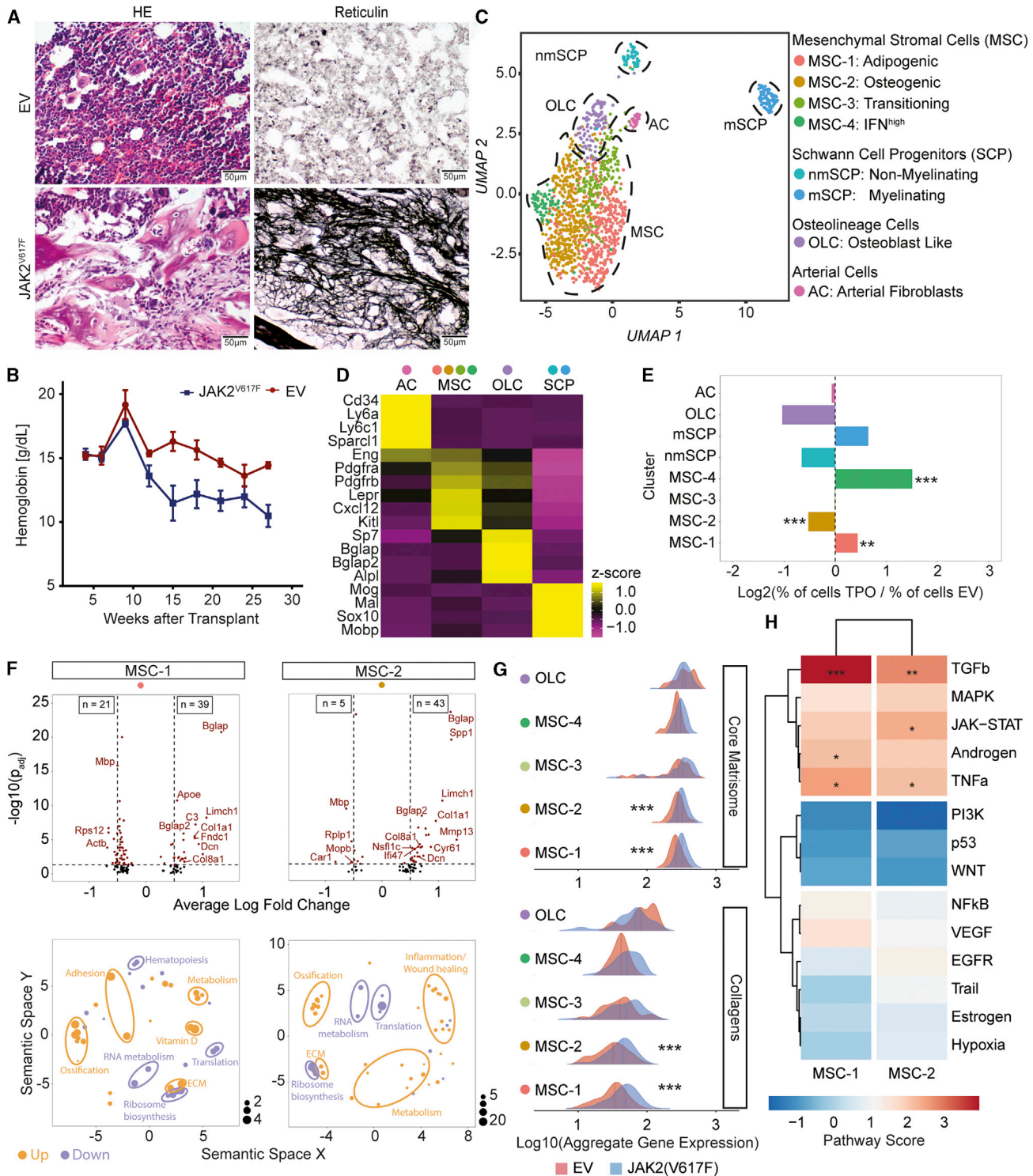


Figure 4. Mesenchymal stromal cells -1 and -2 are reprogrammed in JAK2^{V617F}-induced primary myelofibrosis

(A) Representative HE and reticulin staining of JAK2^{V617F}-induced fibrosis or control (EV, n = 4 mice per condition). Scale bar, 50 μ m.

(B) Hemoglobin levels (mean \pm SEM). Two-way ANOVA with post hoc pairwise t test was used.

(C) UMAP of non-hematopoietic BM cells (n = 1,292 cells).

(D) Top marker genes. Wilcoxon rank-sum test, p < 0.01. A full list of marker genes and corresponding GO terms is provided in Table S2.

(E) Bar plot of cells number in JAK2^{V617F} versus control (EV) after normalization to total number. Fisher's exact test with Bonferroni correction was used.

(legend continued on next page)

(Figure 3E). In pre-fibrosis, MSCs are characterized by downregulated hematopoiesis support (MSC-3 and -4) and MSC characteristics (MSC-1, -2, -3). Even at this early time point, genes defining non-collagenous ECM proteins were significantly upregulated mainly in MSC-1 and -2, the fibrosis-driving cells. In overt fibrosis, MSCs showed highly significant downregulation of hematopoiesis support, MSC characteristics, and strong upregulation of ECM proteins (in all MSC clusters) and collagen (in MSC-1 and -2).

By comparing the differential expression signature of our single cell data with 14 signatures of pathway perturbation in pre-fibrosis and fibrosis (pathway responsive genes [PROGENY] analysis; Schubert et al., 2018), we detected increased activity of pro-inflammatory and pro-angiogenic pathways, specifically tumor necrosis factor (TNF)- α , and also of the JAK-STAT pathway, in fibrosis-driving MSC-1 and -2 (Figure 3F). Interestingly in pre-fibrosis, pro-fibrotic TGF- β signaling was significantly decreased in MSC-1 and -2, while in fibrosis it showed the most extreme upregulation (Figure 3F). The TGF- β pathway, considered to be the master regulator of fibrosis (Meng, Nikolic-Paterson and Lan, 2016), thus seems to play a central role in BM fibrosis but is not one of the earliest events, which are rather inflammation driven.

Single-cell analysis of niche cells confirms MSC-1 and -2 as fibrosis-driving cells and expansion of mSCPs in JAK2^{V617F}-induced myelofibrosis

We validated our findings by using retroviral expression of the JAK2^{V617F} mutation, which is the most common mutation in patients (Mullally et al., 2012; Schneider et al., 2017). After 24 weeks, mice developed severe fibrosis (Figure 4A), low hemoglobin levels, and high platelets (Figure 4B; Figure S4A).

Single cell RNA-seq recovered 1,292 cells non-hematopoietic cells, with an average of 1,000 genes per cell (Table S1). Exactly the same eight populations identified in the ThPO-induced BM fibrosis model were detected (Figure 4C; Figure 4D cf. Figure 1D; Figures S3B–S3D): (1–4) MSCs (MSC-1: adipogenic, MSC-2: osteogenic, MSC-3: transition, MSC-4: interferon high, (5 and 6) Schwann cell precursors (SCPs; 1: non-myelinating SCPs, nmSCPs; 2: myelinating SCPs, mSCPs), (7) osteoblastic lineage cells (OLCs), and (8) arterial fibroblasts (ACs). Cells from all identified populations were present in both the JAK2^{V617F}-induced fibrosis and in non-fibrotic control mice. The integration of all cells indicated an expansion of MSC-1, MSC-4 (interferon-primed), and mSCPs in fibrosis compared to control (Figure 4E). The expansion of mSCPs was comparable to ThPO-induced BM fibrosis, again highlighting the role of glial cells in MPNs.

JAK2^{V617F} induces a phenotypic switch toward myofibroblasts and osteoblasts in MSC-1 and -2

MSC-1 and -2 and OLCs expressed the highest number of differentially expressed genes compared to the control condition (Figure 4F). MSC-1 and -2 were characterized by a strong osteogenic signature (ossification) in line with the advanced fibrosis

grade (MF3). In MSC-1 and -2 the strong upregulation of *Bglap* (bone gamma carboxylglutamate protein, also known as Osteocalcin) indicated an osteogenic differentiation bias. In MSC-2, *Spp1* (Secreted Phosphoprotein 1; also known as Osteopontin) was significantly upregulated. MSC-2 showed a strong inflammation/wound healing signature. MSC-1 and -2 further acquired a “myofibroblast” phenotype (upregulation of *Limch1*; *Dcn*) and expression of *Col1a1*, *Col8a1*, *Fndc1* (Table S3).

Our data show that MSC-1 and -2 in JAK2^{V617F}-induced BM fibrosis acquire an osteogenic and myofibroblast phenotype with loss of MSC progenitor characteristics. SCPs and ACs only showed few changes in their transcriptome in JAK2^{V617F}-induced PMF (Figure S4E). Exactly as observed in the ThPO-model of BM fibrosis, the expanded mSCP population was characterized by expression of the fibrosis-relevant genes *Il33* and *Ptgds* (Figure S4F).

MSC-1 and MSC-2 showed the highest upregulation of ECM proteins, in particular, “core matrisome,” collagen, and glycoproteins in myelofibrosis, confirming that these two MSC populations are the cellular drivers of fibrosis and acquire myofibroblast characteristics (Figure 4G). The significantly upregulated pathways in MSC-1 and -2 were TGF- β , TNF- α , and also JAK-STAT signaling, exactly as seen in the ThPO model, highlighting the importance of these pathways in BM fibrosis (Figure 4H).

Transcriptionally inferred cellular interactions decrease in pre-fibrosis while niche cells show a self-supporting network in fibrosis

We aimed to dissect how cellular interactions within the niche affect the perturbation of signaling pathways detected in fibrosis by employing CellphoneDB (Efremova et al., 2020; Túrei et al., 2016). Most ligand-receptor interactions were markedly decreased in ThPO-induced pre-fibrosis (Figure 5A; Table S5). In fibrosis (ThPO-induced), an overall decrease of cellular interactions was detected, while interactions between OLCs and SCPs increased. Interactions involving fibrosis-driving MSC-1 and MSC-2 showed distinct upregulation, indicating their activation as fibrosis-driving cells (Figure 5A). In the JAK2^{V617F} dataset, a strong upregulation of intercellular communication between all niche populations was observed (Figure 5A). These findings support the hypothesis of a progressive reprogramming of the niche in fibrosis: niche populations first lose their physiological interactions and are then remodeled into a self-supporting network in advancing fibrosis.

We quantified the absolute number of interactions for each unique ligand and ranked them by their absolute frequency (Figure 5B). ECM proteins (*Col1a1*, *Fn1*) and integrins involved in cell-ECM-interactions (*Itgb1*, *Itga1*, *Itgav*) were among the top hits. *Tgfb1*, *Egfr*, and *Nfkb1* were also among the top 10 most abundant ligands. We next focused on interactions involving fibrosis-driving MSC-1 and -2 and *Tgfb1* as a master switch in fibrosis (Figure 5C, first and second panel). Interestingly, MSCs themselves were predicted to be a main source of *Tgfb1*-driven

(F) Volcano plot; Wilcoxon rank-sum test, two tailed; calculated per cluster between JAK2^{V617F} and JAK2^{WT} (top panel). Associated gene ontology terms (biological processes; BP) plotted semantically (bottom panel) are shown. (For a complete list of GO-terms and corresponding genes, see Table S3.)

(G) Ridgeline plot for matrisome gene sets in MSC and OLC clusters (JAK2^{V617F}; blue versus control; red) condition. Competitive gene set enrichment analysis was used.

(H) PROGENY analysis of MSC-1 and MSC-2. Sampling based permutation (10,000 permutations). Pathway activity scores as Z scores are shown. See also Figure S4 and Tables S1, S2, S3, and S4.

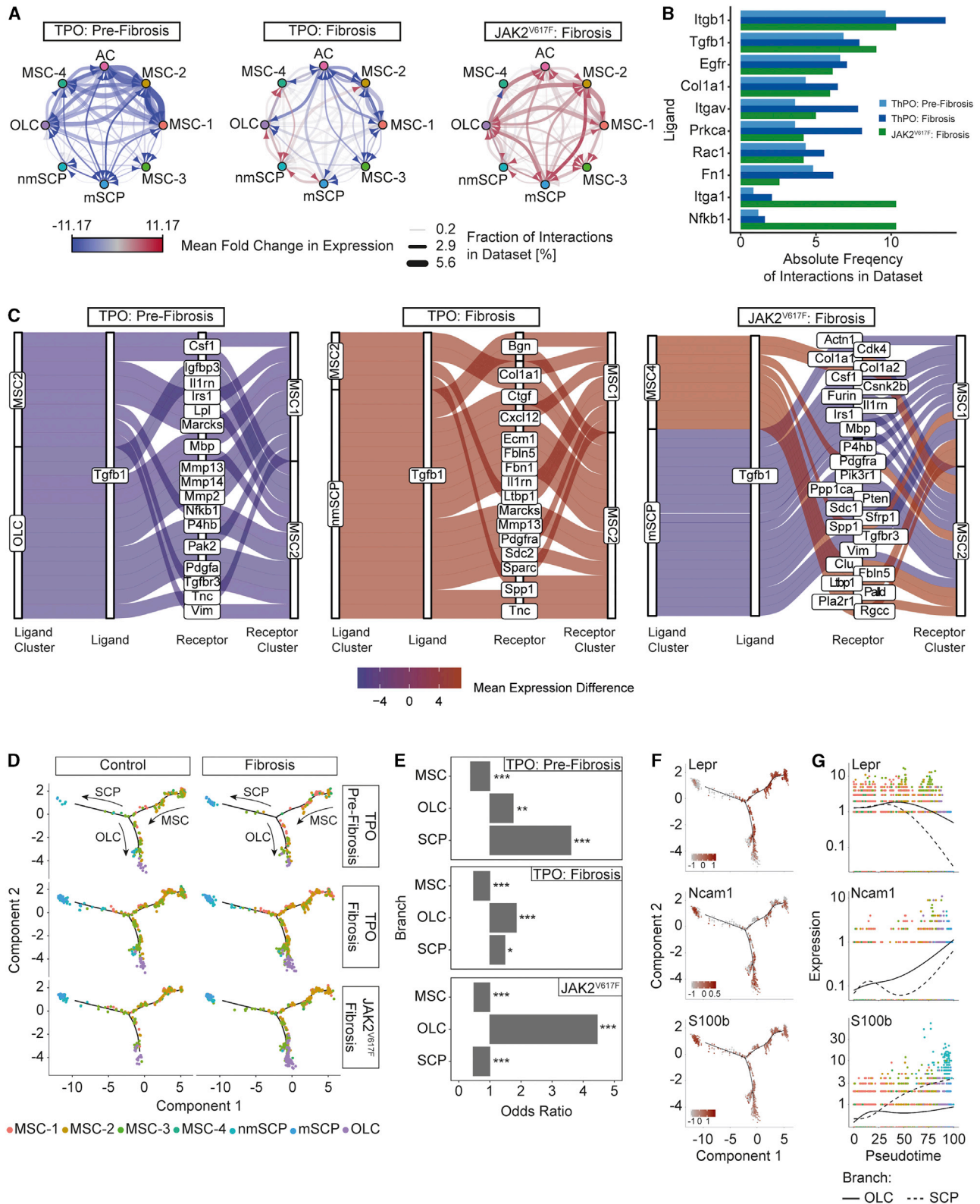


Figure 5. Tgfb1-driven cellular interaction and biased differentiation of MSCs in MPN

(A) Network plot of ligand-receptor activity in control and fibrosis.

(B) Bar plot of top 10 most abundant ligands in all inferred ligand-receptor interactions per dataset. Datasets are shown side by side (ThPO: pre-fibrosis, light blue; ThPO: fibrosis, dark blue; JAK2^{V617F}: fibrosis, green).

(legend continued on next page)

cellular communication and showed upregulation of auto- and paracrine Tgfb1 signaling in manifest fibrosis. Tgfb1-mediated signals between OLCs and MSC-1/2 decreased over time, whereas those originating from SCPs increased. This is particularly interesting as Schwann cells have been described to participate in BM TGFβ signaling (Yamazaki et al., 2011). In JAK2^{V617F}-induced myelofibrosis an upregulation of Tgfb1 signaling in the niche was also observed. Our findings suggest that niche intrinsic TGFβ signaling contributes to the overall reprogramming of MSC-1 and MSC-2 in fibrosis.

MSCs have higher differentiation propensity toward SCPs and osteoblasts in PMF

To understand the differentiation capacities of MSCs in fibrosis, we performed cell-fate trajectory analysis and identified a transcriptional continuum of the 4 MSC populations. SCPs and OLCs represented two distinct differentiated cell populations (terminal branch) starting at MSCs (Figure 5D). The trajectory implied a transition from MSC-1 and MSC-2 through MSC-3, as a transitory state, to one of the two terminal branches (Figure S5A). MSC-2, as osteogenic primed MSCs, showed the highest tendency toward osteoblastic differentiation (Figure 5D) and OLCs increased in fibrosis (Figure 5E). Interestingly, in the ontogeny of the BM HSC niche, some MSCs expressing Nestin share a common origin with sympathetic peripheral neurons and also glial cells. This might explain why some MSCs retain the plasticity to differentiate into glial cells/SCPs and Gli1⁺ cells can also be found in the SCP cluster ((Cai et al., 2017); cf. Figure 2D). To validate differentiation of MSCs into SCPs, we applied published differentiation protocols. MSCs in the differentiation condition showed a significant upregulation of S100b and p75 neurotrophin receptor (p75ntr), indicating differentiation into SCPs (Figure S5B). We thus hypothesize that mutant (and fibrosis-inducing) HSCs can induce the terminal differentiation of MSCs into (1) matrix-secreting myofibroblasts, (2) osteolineage cells, or (3) to a lower extent Schwann cell precursors/Schwann cells.

Branched expression analysis modeling (BEAM) (Qiu et al., 2017) revealed a gradual loss of MSC-specific markers along the trajectory, which was particularly pronounced in the transdifferentiation toward SCPs (LepR). At the same time these cells acquire expression of S100b, a well-known marker for the Schwann cell lineage, at progenitor stages, which is also expressed on MSCs differentiated into SCPs (Figure 5F). The expression of S100b at a later stage is associated with increasing expression of Ncam1 (CD56) in both OLCs and SCPs (Figures 5F and 5G). Projecting the measured expression levels to the pseudotime trajectory confirmed a rather sparse pattern of cells differentiating toward SCPs, in particular, compared to OLCs (Figures 5F and 5G).

We next wondered whether the strong bias toward OLCs and myelinating SCP differentiation is reflected in patient samples. Systematic analyses of BM biopsies showed that spindle-shaped CD56/NCAM positive cells are activated from the endosteal niche (normal location) in the progression of BM fibrosis when they can be found abundantly in the marrow (Figures S5C–S5E, Figures S5D and S5E). S100b positive cells in control BMs (MF0) were mostly located in a periarterial localization (Figure S5F). In advanced MF, they were mobilized from their normal niche and were increased in their frequency (Figures S5F and S5G). Double immunohistochemistry for IL-33 and S100b confirmed occasional double positive spindle-shaped cells in the BM, as observed in our scRNA-seq data (Figure S5H).

Single-cell RNA-seq of the BM niche in PMF patients and controls confirms the molecular reprogramming of fibrosis-driving MSCs

Next, we validated our findings in clinical patient samples. One of the major challenges in late-stage myelofibrosis is that accessibility of liquid BM by aspiration is often limited (dry tap), and hematopoietic tissue for diagnosis is only available in the form of a BM biopsy. We received ~5 mm long pieces of biopsies (excess material not needed for diagnostics; Figure S6A) of two control patients (Figure 6A; Figure S6B) and 1 patient with JAK2^{V617F} MPNs/PMF (VAF 13% in BM; MF grade 2–3; Figure 6A; Figure S6C). Stromal cells were enriched from BM biopsies after crushing and flow-based cell sorting of CD45[−]/CD71[−]/CD235a⁷/AAAD[−] cells (Figure S6D; Figure 6B; Table S1).

Unsupervised clustering identified 5 distinct major cell populations (Figure 6B): two hematopoietic and three stromal cell clusters. Stromal cell clusters were defined as (1) MSCs, (2) fibroblasts (Fib), and (3) Schwann cells (SC). MSCs were characterized, in line with the murine data, by high expression of Leptin receptor (LEPR), platelet-derived growth factor receptor b (PDGFRB), and CXCL12 (Figure 6C). Fibroblasts do not express these MSC-specific markers but express ECM proteins as collagen 1a1 (COL1A1) and fibronectin-1 (FN1); (Figure 6C). The Schwann cell cluster showed concordance with the murine dataset, in particular, in expression of myelin-associated oligodendrocyte basic protein (MOBP). The hematopoietic clusters were characterized by megakaryocyte-specific (Meg) markers (PF4, PPBP, and ITGA2B) and markers for myeloid cells (S100A8, ELANE, MPO); (Figure 6C). Importantly, all cell clusters were present in the control and PMF sample in comparable distribution (Figure 6B).

Strikingly, MSCs transcriptionally showed loss of their core cellular characteristics as (1) downregulated niche and hematopoiesis support and (2) decreased MSC multipotent progenitor status (MSC signature; Figure 6D). They further showed

(C) Top 20 deregulated interactions mediated by Tgfb1 targeting MSC-1 and MSC-2. Interactions ordered based on difference in mean LR expression between fibrosis and control. (For a full list of inferred ligand-receptor interactions, see Table S5.)

(D) Reconstructed cell differentiation trajectory of MSC populations.

(E) Bar plot of numerical changes between fibrosis and control in respective branches as identified in pseudotime analysis. Fisher's exact test with Bonferroni correction was used.

(F) Expression levels of highlighted genes projected onto differentiation trajectory in pseudotime space.

(G) Expression levels of indicated genes with respect to their pseudotime coordinates. Black line indicates differentiation trajectory toward OLC branch and dotted lines toward SCP branch.

See also Figure S5 and Table S5.

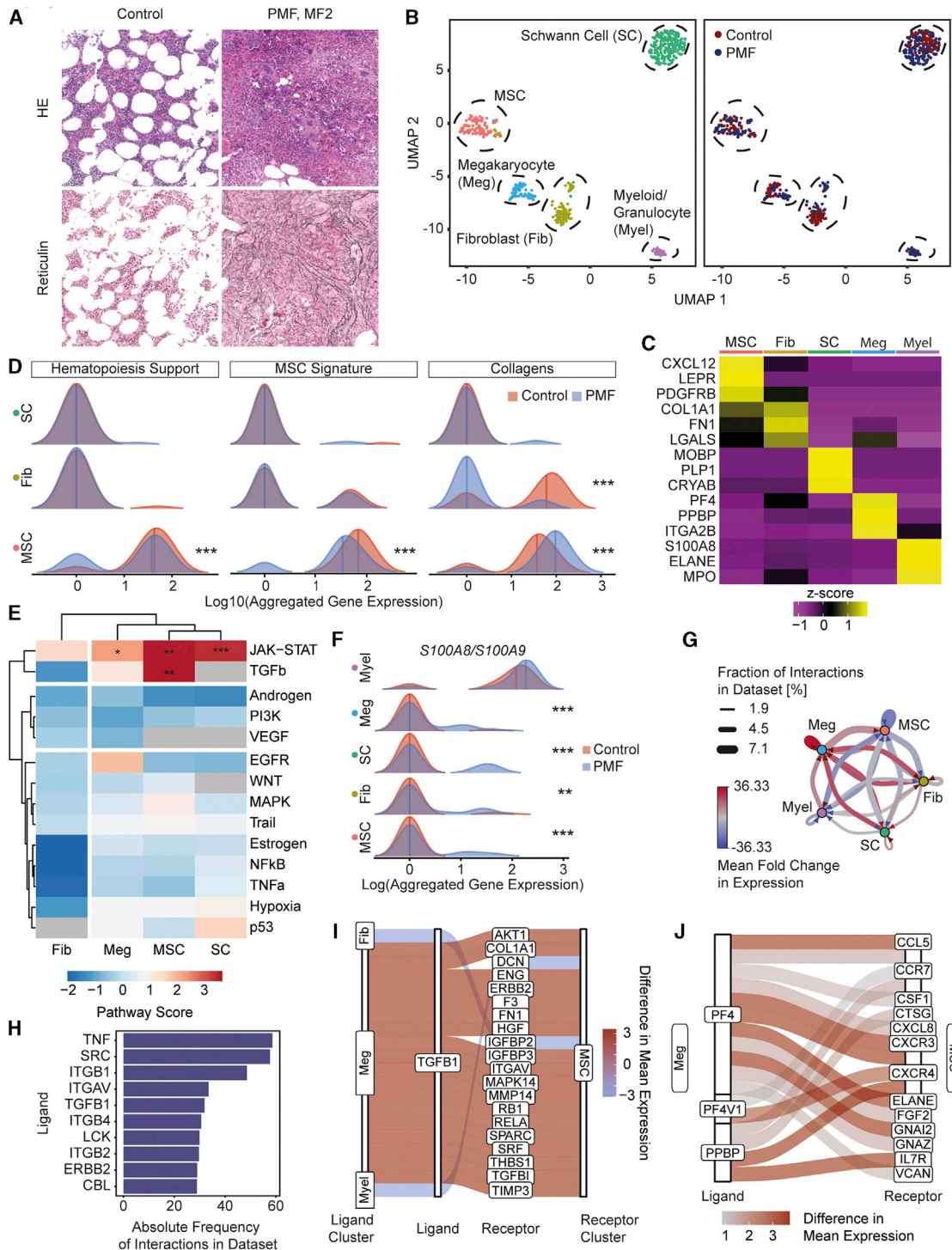


Figure 6. MSCs are fibrosis-driving cells in patients characterized by upregulation of S100A8/A9

(A) Diagnostic BM images of the patients. Representative H&E and reticulin stainings. For additional images (all controls) and detailed patient characteristics, see Figure S5.

(B) UMAP of cells in 1 PMF patient (MF2, n = 243 cells) and two control patients (MF0, n = 255 cells). In the left panel, cells are color coded by their annotated cellular identity, and in the right panel, by their patient source.

(C) Top marker genes. Wilcoxon rank-sum test, $p < 0.01$.

(D) Ridgeline plot comparing PMF (blue) versus control (red) condition. Competitive gene set enrichment analysis was used.

(E) PROGENy analysis. Sampling-based permutation (10,000 permutations). Pathway activity scores are given as Z scores.

(legend continued on next page)

significant upregulation of ECM proteins, specifically collagens, in PMF compared to normal BMs. Exactly as observed in the murine models, significantly upregulated pathways in those cells were JAK-STAT and TGF- β in MSCs as fibrosis-driving cells (Figure 6E).

The alarmin heterocomplex S100A8/S100A9, which can be considered a myeloid marker and is highly expressed in myeloid cells, was significantly upregulated in non-hematopoietic stromal cells that do not show S100A8/S100A9 expression in steady state (Figure 6F), in line with our murine datasets (Figure S6E). Previous data indicate that upregulated S100A8/S100A9 expression (and release) can be a stress response, impair normal hematopoiesis, and induce genotoxic stress and might thus reflect disease progression (Schneider et al., 2016; Vainchenker and Plo, 2016; Yang et al., 2016; Zambetti et al., 2016; Ribezzo et al., 2019). There is indication that S100A8/S100A9 exerts its biological effects specifically in the vicinity of the producing cell (Vogl et al., 2018). In PMF, this means that MSCs upregulate the alarmin complex and mainly affect HSCs in their vicinity but also megakaryocytes and Schwann cells, which in turn start to express S100A8/S100A9.

The S100A8/S100A9-driven cross-talk in PMF patients originated strongly from myeloid cells. Importantly, the interaction with almost all niche cells and specifically MSCs was increased in PMF (Figure S6F). This provides further evidence for the broad effect of S100A8/A9 on populations involved in fibrotic transformation. In PMF, megakaryocytes dominated cellular interactions with all niche cells while other hematopoietic-niche cell interactions rather decreased (Figure 6G). As seen in the murine models, megakaryocyte-derived TGFB1 signals were highly upregulated (Figure 6H) while TGFB1 signals from other clusters, such as fibroblasts and myeloid cells, were downregulated in PMF (Figure 6I). Other megakaryocyte-derived mediators with implication in PMF were also upregulated: PF4 (CXCL4), its homolog PF4V1 and platelet-basic protein precursor (PPBP) (Schneider et al., 2017; Gleitz et al., 2020). Signaling through pro-fibrotic receptors as VCAN and GF2 was also upregulated in PMF compared to controls (Figure 6J). This provides evidence that the interaction between megakaryocytes and fibrosis-driving MSCs is central in the priming and fibrotic transformation of MSCs.

The alarmin S100A8/S100A9 complex is systemically increased in MPNs and stromal alarmin expression marks the onset and progression of BM fibrosis

Our data in patient samples and murine models indicated that S100A8/S100A9 expression in MSCs is already upregulated in pre-fibrosis and significantly increased in fibrotic stages in almost all niche cells, suggesting S100A8/S100A9 as a sensitive marker for disease/fibrosis progression. We thus asked whether

S100A8, one subunit of the heterodimeric complex, is also secreted and can mark the progression of BM fibrosis in patients. We quantified S100A8 in plasma samples (peripheral blood) from MPN patients by ELISA (Figure S7A). S100A8 was significantly increased in MPN patients (Figure 7A) and demarcated the transition from MF0 to MF1 and higher MF grades, indicating S100A8 as a sensitive marker for fibrosis onset or progression in PMF when follow-up samples are taken (Figure 7B). The S100A8 plasma concentration did not correlate with white blood cell counts, emphasizing that the elevated concentration is not only caused by the disease-specific myeloproliferation (Figure S7B). In previous work, we linked increased S100A8 expression in the stroma (in MDS) to decreased hematopoiesis support (Ribezzo et al., 2019). We performed immunohistochemistry for S100A8 on BM biopsies (Figures S7C and S7D). S100A8⁺ hematopoietic cells were expanded in MPNs in MF grade 0–1 but rather decreased in MF grade 2–3 due to progressing fibrosis (Figure 7C). Detailed analysis of S100A8 expression in the BM revealed distinct staining and distribution patterns, which we defined as four grades of S100A8 expression (Figures 7D and 7E): in grade 0 the S100A8 expression is limited to hematopoietic/myeloid cells, in grade 1 interstitial S100A8 staining is detected, in grade 2 distinct patches of stromal cells stain positive for S100A8, in grade 3 the S100A8 expression is significantly reduced in hematopoietic cells, but dense patches of positively stained stromal cells can be found (Figure S7D). Control BMs were consistently graded as grade 0 while, in particular, S100A8 grade 2 marked the progression of BM fibrosis, suggesting that stromal expression of the heterodimeric S100A8/S100A9 alarmin complex is a sensitive marker for disease progression (Figure S7E).

S100A8/S100A9 is a therapeutic target in PMF

To determine whether the alarmin complex is a therapeutic target in MPNs associated with fibrosis, we tested Tasquinimod in the murine JAK2^{V617F} MF model (Figure S7F). Tasquinimod binds to the S100A8/S100A9 alarmin heterodimer and impedes its interaction with TLR4 and RAGE receptors (Isaacs et al., 2006). Tasquinimod treatment ameliorated the myeloproliferation in JAK2^{V617F} mice comparable to leukocyte, hemoglobin, and platelet counts in controls (Figure 7F; Figures S7G and S7H). Severe splenomegaly, which is a major clinical manifestation in PMF patients, was observed in vehicle-treated JAK2^{V617F} mice but completely normalized with Tasquinimod treatment (Figures 7G and 7H). Importantly, Tasquinimod treatment in JAK2^{V617F} mice significantly reduced the fibrosis grade and restored the BM architecture in MPNs (Figure 7I; Figures S7I–S7J).

To investigate the direct effect of Tasquinimod on the fibrotic transformation of MSCs, we induced the fibrotic transformation

(F) Ridgeline plot of S100A8/A9 expression in PMF (blue) or control (red). Significance estimated by modeling the dropout rate as a binomial process with the observed dropout rate per condition as estimator of *p* for both conditions, respectively.

(G) Network plot of ligand-receptor activity in PMF compared to control.

(H) Bar plot of top 10 most abundant ligands in all inferred ligand-receptor interactions.

(I) Sankey plot of top 20 deregulated TGFB1-mediated ligand-receptor interactions. The absolute difference in mean LR expression was used as a metric for the extent of deregulation.

(J) Sankey plot of top 20 deregulated ligand-receptor interactions mediated by PF4, PF4V1, or PPBP. The absolute difference in mean LR expression was used as a metric for the extent of deregulation.

See also Figure S6 and Tables S1, S2, S3, S4, and S5.

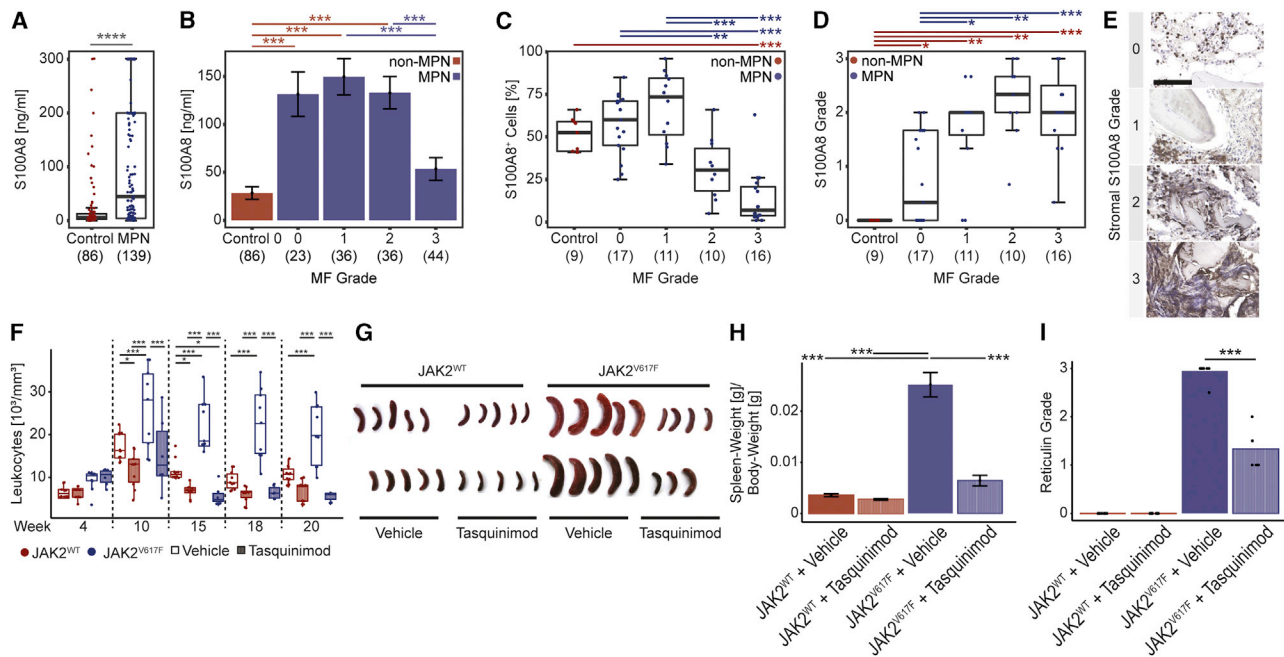


Figure 7. Spatial kinetics of S100A8/S100A9 detects disease progression in MPN and their pharmacological targeting ameliorates the disease

(A) ELISA of S100A8 (and S100A9) in MPN (blue) and controls (red) plasma. Two-tailed, two-sample Welch test was used.
 (B) ELISA of S100A8 (and S100A9) in MPN with different MF grades (blue) and controls (red) plasma. Mean \pm SEM. One-way-ANOVA with post hoc Tukey's was used.
 (C) Frequency of S100A8⁺ cells BM biopsies; n = 64 patients. One-way-ANOVA with post hoc Tukey's HSD was used.
 (D and E) Grading of S100A8 in the non-hematopoietic compartment in BM biopsies. Scale bar, 100 μ m. n = 64 patients. Kruskal-Wallis H test with post hoc Wilcoxon rank-sum test was used. p values were adjusted for multiple hypothesis testing by the Holm-Bonferroni method.
 (F) White blood cell counts of WT mice transplanted with either *JAK2*^{V617F} (blue) or *JAK2*^{WT} overexpressing HSPCs (red) each either treated with Tasquinimod 30 mg/kg/day or vehicle control. Two-way repeated ANOVA pairwise comparisons were analyzed by estimated marginal means.
 (G) Splens at sacrifice as indicated.
 (H) Relative spleen weights. Mean \pm SEM. One-way-ANOVA with post hoc Tukey's HSD.
 (I) Reticulin (MF) grade. Kruskal-Wallis H test with post hoc Wilcoxon rank-sum test.
 See also [Figure S6](#).

of isolated primary MSCs by addition of TGF- β as a strong pro-fibrotic stimulus in the absence or presence of Tasquinimod. The addition of TGF- β induced the differentiation of MSCs into α -SMA-positive myfibroblasts. Tasquinimod significantly reduced the frequency of α -SMA positive myfibroblasts but did not completely block this important step in the fibrotic transformation.

These results provide strong indication that S100A8/S100A9 plays a central role in the fibrotic transformation, directly on MSCs but also through the hematopoietic-stromal cross-talk, and that its pharmacological targeting ameliorates both the MPN phenotype but also fibrosis and exerts effects on stromal cells and the mutant hematopoietic clone.

DISCUSSION

Our findings supplement the picture of the BM microenvironment in the presence of a malignant hematopoietic MPN clone, which induces a regenerative but pro-fibrotic environment leading to (mal-)differentiation of distinct MSC populations with loss of their normal function. MSCs are increasingly recognized as a major source of fibrosis-associated myfibroblasts in various or-

gans (El Agha et al., 2017). These findings are almost solely based on genetic fate tracing, which is the gold-standard approach for studying cell-fate switching in response to pathological stimuli (Kramann et al., 2015; Schneider et al., 2017). Here, we applied single-cell RNA-seq to better understand fate switching of distinct precursor cells/MSC populations during injury induced by a malignant clone. Several key observations were only possible due to the single cell-level resolution of our study, highlighting the power of single-cell technologies in understanding disease pathology and biomarker identification for pre-fibrotic stages.

We demonstrate that two distinct MSC populations (MSC-1 and MSC-2) are the main drivers of BM fibrosis in two well-established models. These two MSC populations are LepR⁺, adipogenic-, or osteogenic-biased progenitor populations under steady-state conditions with high expression of *Cxcl12*, indicating their hematopoiesis-supporting capacity. Importantly, the different MSC populations identified in our study are in line with the four different MSC populations described before using either lineage-negative selection as in our approach; (Baryawno et al., 2019) or sort purification of LepR-positive cells (Tikhonova et al., 2019), respectively. Gli1⁺ cells on the single-cell level are

MSCs, which are enriched for MSC-1 and -2, as fibrosis-driving cells and also in part have SCP character. These data highlight that some MSCs are also derived from neural crest and thus have a common origin with sympathetic peripheral neurons and glial cells, reflected by their expression profile (Isern et al., 2014). Given their expression profile and the pseudotime analysis, MSC-1 and -2 seem to be (multipotent) mesenchymal progenitor cells, which means mesenchymal cells that are capable of differentiating into a limited number of cell types. These two progenitor populations are the predominant *Col1a1*-producing cells in overt BM fibrosis. Importantly, collagen I is considered the hallmark ECM protein of fibrosis. Our data identified these two populations as key drivers of myelofibrosis and add novel insight into the role of these populations in this most extensive form of remodeling of the BM microenvironment. The functional characterization of sort-purified MSC-1 and -2 confirmed the transcriptional data on the single-cell level and demonstrated their progenitor profile. Thus, the proposed antibody panel for enrichment of MSC-1 and -2 is also interesting for approaches requiring an enrichment of more immature progenitor cells, e.g., in regenerative medicine. It is important to note that in all approaches we were able to cover the majority of cell populations known to be part of the hematopoietic niche, yet only MSCs proved to be responsive to the malignant hematopoietic clone with regards to ECM production. This makes therapeutical targeting of the niche highly attractive (Curto-Garcia, Harrison, and McLornan 2020; Méndez-Ferrer et al., 2020; Schneider et al., 2017).

We demonstrate that MSCs are functionally reprogrammed in fibrosis with loss of their progenitor status and normal function in the BM microenvironment. We show that the reprogramming of MSCs is a stepwise process, which starts with loss of “MSC characteristics” in all 4 MSC populations, not only in the fibrosis-driving ones, already in the pre-fibrotic phase. This indicates that all MSC populations react to the fibrosis-inducing hematopoietic clone while only MSC-1 and -2 are capable of differentiation into ECM-producing myofibroblasts. Interestingly, all MSC subsets lose their hematopoiesis support over time and contribute to the production of non-collagenous ECM with scaffolding function for collagen fibrosis. Our data indicate that TGF- β plays a central role in the reprogramming as addition of TGF- β to fibrosis-driving MSCs leads to downregulation of CXCL12 with central role in hematopoiesis support. The increased differentiation of all MSC populations in BM fibrosis can be interpreted as excessive maldifferentiation, in particular, the osteogenic differentiation, which leads to bone formation in the marrow. Maldifferentiation of MSCs has also been described in other organs under reactive and regenerative conditions, e.g., the heart (Breitbach et al., 2007) and the kidney (Kunter et al., 2007). In the persistence of a malignant, fibrosis-inducing hematopoietic clone, MSCs are continuously pushed toward differentiation, which leads to a vicious cycle of loss of tissue function and scarring with high resemblance to solid organ fibrosis.

Inflammation plays a critical role within this vicious circle and we here demonstrate that the alarmin heterodimer S100A8/S100A9 is an important pro-inflammatory player in MPNs with distinct kinetics: strong expression in hematopoietic cells demarcates the myeloproliferative phase and expression in the stroma demarcates the fibrotic progression. Myeloid cells ex-

press S100A8/S100A9 at baseline (as a marker) but do not show upregulation in fibrosis/MPNs. Stromal cells, however, do not express S100A8/S100A9 at steady state but upregulate the expression in disease. In previous work, we linked increased S100A8/S100A9 expression in the stroma (where it is not expressed in healthy individuals) to decreased hematopoiesis support (Ribezzo et al., 2019), underlining that S100A8/S100A9 might be a good marker for the reprogramming of the stroma from hematopoiesis support toward fibrotic transformation, in particular, if followed up in patients over time. Strikingly, Tasquinimod ameliorated the MPN phenotype and fibrosis, suggesting that it affects both the mutated hematopoietic clone but also the fibrotic transformation. Our data indicate that pharmacological targeting of S100A8/S100A9 has huge translational value providing first evidence for the design of clinical phase I studies.

Limitations of study

The aim of our study was to investigate changes in non-hematopoietic cells of the BM in the progress of myelofibrosis. It is well accepted that the isolation process of niche cells is associated with a bias toward certain cell types (Baccin et al., 2020). Thus, niche populations can be underrepresented. The number of tools for inferring ligand-receptor interactions is rapidly increasing. The overlap between the databases, however, is relatively small. Identified interactions will need to be validated in the future and used for prospective curation of the available tools. Finally, liquid BM frequently cannot be aspirated in advanced myelofibrosis. Hence, purifying a high number of cells for scRNA-seq is very challenging. Therefore, the data generated here will be validated in a larger cohort in the future.

STAR★METHODS

Detailed methods are provided in the online version of this paper and include the following:

- KEY RESOURCES TABLE
- RESOURCE AVAILABILITY
 - Lead contact
 - Materials availability
 - Data and code availability
- EXPERIMENTAL MODEL AND SUBJECT DETAILS
 - Animal studies
 - Human studies
 - Cell lines and cell culture
- METHOD DETAILS
 - Viral transduction
 - Induction of myelofibrosis by overexpression of ThPO or JAK2^{V617F}
 - Isolation of bone marrow stromal cells for scRNA sequencing
 - FACS-staining and sorting of bone marrow stromal cells for scRNA sequencing
 - Isolation of Gli1⁺ stromal cells in homeostasis for scRNaseq
 - Single cell library preparation and sequencing
 - Single cell RNA seq data analysis of ThPO and Jak2 mouse models

- Integration of single cell RNA seq data of Gli1 sorted cells
- Single cell RNA seq data analysis of human samples
- Reconstructing cell development trajectories
- PROGENy analysis
- Ligand-receptor analysis
- Quantification of S100A8 in human plasma samples
- Histological and immunohistological analysis
- Co-staining of human bone marrow samples for S100b/IL-33
- FACS-staining and sorting of MSC-1/2 and MSC-3/4 for functional analysis
- CFU-F assay
- Growth curve
- Recombinant cytokine stimulation of primary murine stromal cells
- MSC to SCP transition
- Treatment of mice with Tasquinimod
- Treatment of cells with Tasquinimod
- Image processing
- **QUANTIFICATION AND STATISTICAL ANALYSIS**

SUPPLEMENTAL INFORMATION

Supplemental Information can be found online at <https://doi.org/10.1016/j.stem.2020.11.004>.

ACKNOWLEDGMENTS

R.K. was supported by grants from the Deutsche Forschungsgemeinschaft German Research Foundation (DFG; SCHN1188/5-1, SFBTRR219, and SFBTRR57), a grant from the European Research Council (ERC-StG 677448), and a grant from the Interdisciplinary Centre for Clinical Research (IZKF) within the faculty of Medicine at the RWTH Aachen University (O3-11). R.K.S. is an Onco Institute investigator and was supported by grants from the MPN Foundation (2017 MPNRF/LLS Award), a KWF Kankerbestrijding young investigator grant (11031/2017-1, Bas Mulder Award; Dutch Cancer Foundation), and an ERC grant (deFIBER; ERC-StG 757339). This work was in part supported by grants of the Deutsche Forschungsgemeinschaft (DFG) (German Research Foundation) to R.K. (KR 4073/9-1), R.K.S. (SCHN1188/6-1), T.B. (BR1782/5-1), S.K. (KO2155/7-1), and I.C. (GE2811/4-1) within the clinical research unit CRU344. R.K., I.G.C., and R.K.S. are members of the E:MED Consortia Fibromap funded by the German Ministry of Education and Science (BMBF). P.B. was financially supported by DFG (SFB/TRR57, SFB/TRR219, BO3755/6-1), BMBF (STOP-FSGS-01GM1901A), and the IZKF (O3-2). N.B.L. was supported DFG (BA 6349/1-1). H.F.E.G. was supported by the European Union's Horizon 2020 research and innovation program under a Marie Curie-Sklodowska grant (707404 LEaDing Fellow). I.G.C. was supported by an IZKF grant (E8-15). We thank the team of the Translational Research Unit of the Institute of Pathology of the University of Bern as well as the team of the Institute for Clinical Chemistry, Molecular Diagnostics and Pathology (PARTS) at Erasmus Medical Center, Rotterdam. We further would like to thank Remco Hoogenboezem for excellent support in processing raw sequencing data for downstream analysis.

AUTHOR CONTRIBUTIONS

N.B.L. and H.F.E.G. designed and carried out experiments, analyzed results, and wrote the manuscript. L.R. performed the biocomputational analysis, interpreted the results, and wrote the manuscript. I.A.M.S., J.S.N., S.F., C.K., U.S.A.S., B.B., and E.B. performed experiments, analyzed, interpreted data, and reviewed the manuscript. G.B., H.K., I.G., P.K., T.V., K.H.L. Y.B., P.B., E.W.-Y.T., T.H.B., S.K., and M.C. selected patient specimens, performed stainings on murine and human tissues, and reviewed the manuscript. R.K., I.G.C., and R.K.S. obtained funding, designed the study, performed experi-

ments, analyzed data, and wrote the manuscript. All authors provided critical analysis of the manuscript.

DECLARATION OF INTERESTS

The authors declare no competing interests.

Received: November 15, 2019

Revised: August 18, 2020

Accepted: November 9, 2020

Published: December 9, 2020; Corrected online: December 10, 2020

REFERENCES

- Alvarez, M., Shen, Y., Giorgi, F., et al. (2016). Functional characterization of somatic mutations in cancer using network-based inference of protein activity. *Nat Genet* 48, 838–847.
- Baccin, C., Al-Sabah, J., Velten, L., Helbling, P.M., Grünschlager, F., Hernández-Malmierca, P., Nombela-Arrieta, C., Steinmetz, L.M., Trumpp, A., and Haas, S. (2020). Combined single-cell and spatial transcriptomics reveal the molecular, cellular and spatial bone marrow niche organization. *Nat. Cell Biol.* 22, 38–48.
- Barbui, T., Thiele, J., Gisslinger, H., Kvasnicka, H.M., Vannucchi, A.M., Guglielmelli, P., Orzi, A., and Tefferi, A. (2018). The 2016 WHO classification and diagnostic criteria for myeloproliferative neoplasms: document summary and in-depth discussion. *Blood Cancer J.* 8, 15.
- Baryawno, N., Przybylski, D., Kowalczyk, M.S., Kfoury, Y., Severe, N., Gustafsson, K., Kokkalis, K.D., Mercier, F., Tabaka, M., Hofree, M., et al. (2019). A Cellular Taxonomy of the Bone Marrow Stroma in Homeostasis and Leukemia. *Cell* 177, 1915–1932.
- Breitbach, M., Bostani, T., Roell, W., Xia, Y., Dewald, O., Nygren, J.M., Fries, J.W.U., Tiemann, K., Bohlen, H., Hescheler, J., et al. (2007). Potential risks of bone marrow cell transplantation into infarcted hearts. *Blood* 110, 1362–1369.
- Butler, A., Hoffman, P., Smibert, P., Papalexi, E., and Satija, R. (2018). Integrating single-cell transcriptomic data across different conditions, technologies, and species. *Nat. Biotechnol.* 36, 411–420.
- Cai, S., Tsui, Y.P., Tam, K.W., et al. (2017). Directed Differentiation of Human Bone Marrow Stromal Cells to Fate-Committed Schwann Cells. *Stem Cell Reports* 9, 1097–1108.
- Ceccarelli, Francesco, Turei, Denes, Gabor, Attila, and Saez-Rodriguez, Julio (2020). Bringing data from curated pathway resources to Cytoscape with OmniPath. *Bioinformatics* 36, 2632–2633.
- Curto-Garcia, N., Harrison, C., and McLornan, D.P. (2020). Bone marrow niche dysregulation in myeloproliferative neoplasms. *Haematologica* 105, 1189–1200.
- Decker, M., Martinez-Morentin, L., Wang, G., Lee, Y., Liu, Q., Leslie, J., and Ding, L. (2017). Leptin-receptor-expressing bone marrow stromal cells are myofibroblasts in primary myelofibrosis. *Nat. Cell Biol.* 19, 677–688.
- Durinck, S., Spellman, P., Birney, E., et al. (2009). Mapping identifiers for the integration of genomic datasets with the R/Bioconductor package biomaRt. *Nat Protoc* 4, 1184–1191.
- Efremova, M., Vento-Tormo, M., Teichmann, S.A., and Vento-Tormo, R. (2020). CellPhoneDB: inferring cell-cell communication from combined expression of multi-subunit ligand-receptor complexes. *Nat. Protoc.* 15, 1484–1506.
- El Agha, E., Kramann, R., Schneider, R.K., Li, X., Seeger, W., Humphreys, B.D., and Bellusci, S. (2017). Mesenchymal Stem Cells in Fibrotic Disease. *Cell Stem Cell* 21, 166–177.
- Friedman, S.L., Sheppard, D., Duffield, J.S., and Violette, S. (2013). Therapy for fibrotic diseases: nearing the starting line. *Sci. Transl. Med.* 5, 167sr1.
- Gleitz, H.F.E., Dugourd, A.J.F., Leimkühler, N.B., Snoeren, I.A.M., Fuchs, S.N.R., Menzel, S., Ziegler, S., Kröger, N., Trivai, I., Büsche, G., et al. (2020). Increased CXCL4 expression in hematopoietic cells links inflammation and progression of bone marrow fibrosis in MPN. *Blood* 136, 2051–2064.

- Isaacs, J.T., Pili, R., Qian, D.Z., Dalrymple, S.L., Garrison, J.B., Kyprianou, N., Björk, A., Olsson, A., and Leanderson, T. (2006). Identification of ABR-215050 as lead second generation quinoline-3-carboxamide anti-angiogenic agent for the treatment of prostate cancer. *Prostate* 66, 1768–1778.
- Isern, J., García-García, A., Martín, A.M., Arranz, L., Martín-Pérez, D., Torroja, C., Sánchez-Cabo, F., and Méndez-Ferrer, S. (2014). The neural crest is a source of mesenchymal stem cells with specialized hematopoietic stem cell niche function. *eLife* 3, e03696.
- Ito, H., Yan, X., Nagata, N., Aritake, K., Katsumata, Y., Matsuhashi, T., Nakamura, M., Hirai, H., Urade, Y., Asano, K., et al. (2012). PGD2-CRTH2 pathway promotes tubulointerstitial fibrosis. *J. Am. Soc. Nephrol.* 23, 1797–1809.
- Kotsiou, O.S., Gourgoulis, K.I., and Zarogiannis, S.G. (2018). IL-33/ST2 Axis in Organ Fibrosis. *Front. Immunol.* 9, 2432.
- Kramann, R., Schneider, R.K., DiRocco, D.P., Machado, F., Fleig, S., Bondzie, P.A., Henderson, J.M., Ebert, B.L., and Humphreys, B.D. (2015). Perivascular Gli1+ progenitors are key contributors to injury-induced organ fibrosis. *Cell Stem Cell* 16, 51–66.
- Kunter, U., Rong, S., Boor, P., Eitner, F., Müller-Newen, G., Djuric, Z., van Roeyen, C.R., Konieczny, A., Ostendorf, T., Villa, L., et al. (2007). Mesenchymal stem cells prevent progressive experimental renal failure but maldifferentiate into glomerular adipocytes. *J. Am. Soc. Nephrol.* 18, 1754–1764.
- McCarthy, D.J., Chen, Y., and Smyth, G.K. (2012). Differential expression analysis of multifactor RNA-Seq experiments with respect to biological variation. *Nucleic Acids Res.* 40, 4288–4297.
- Méndez-Ferrer, S., Bonnet, D., Steensma, D.P., Hasserjian, R.P., Ghobrial, I.M., Gribben, J.G., Andreeff, M., and Krause, D.S. (2020). Bone marrow niches in haematological malignancies. *Nat. Rev. Cancer* 20, 285–298.
- Meng, X.-M., Nikolic-Paterson, D.J., and Lan, H.Y. (2016). TGF- β : the master regulator of fibrosis. *Nat. Rev. Nephrol.* 12, 325–338.
- Mullally, A., Lane, S.W., Brumme, K., and Ebert, B.L. (2012). Myeloproliferative neoplasm animal models. *Hematol. Oncol. Clin. North Am.* 26, 1065–1081.
- Naba, A., Clauser, K.R., Ding, H., Whittaker, C.A., Carr, S.A., and Hynes, R.O. (2016). The extracellular matrix: Tools and insights for the “omics” era. *Matrix Biol.* 49, 10–24.
- Qiu, X., Hill, A., Packer, J., Lin, D., Ma, Y.-A., and Trapnell, C. (2017). Single-cell mRNA quantification and differential analysis with Census. *Nat. Methods* 14, 309–315.
- Rampal, R., Al-Shahrour, F., Abdel-Wahab, O., Patel, J.P., Brunel, J.-P., Mermel, C.H., Bass, A.J., Pretz, J., Ahn, J., Hricik, T., et al. (2014). Integrated genomic analysis illustrates the central role of JAK-STAT pathway activation in myeloproliferative neoplasm pathogenesis. *Blood* 123, e123–e133.
- Ribezzo, F., Snoeren, I.A.M., Ziegler, S., Stoelben, J., Olofsen, P.A., Henic, A., Ferreira, M.V., Chen, S., Stalman, U.S.A., Buesche, G., et al. (2019). Rps14, Csnk1a1 and miRNA145/miRNA146a deficiency cooperate in the clinical phenotype and activation of the innate immune system in the 5q- syndrome. *Leukemia* 33, 1759–1772.
- Satija, R., Farrell, J.A., Gennert, D., Schier, A.F., and Regev, A. (2015). Spatial reconstruction of single-cell gene expression data. *Nat. Biotechnol.* 33, 495–502.
- Schneider, R.K., Schenone, M., Ferreira, M.V., Kramann, R., Joyce, C.E., Hartigan, C., Beier, F., Brummendorf, T.H., Gerding, U., Platzbecker, U., et al. (2016). Rps14 haploinsufficiency causes a block in erythroid differentiation mediated by S100A8 and S100A9. *Nat. Med.* 22, 288–297.
- Schneider, R.K., Mullally, A., Dugourd, A., Peisker, F., Hoogenboezem, R., Van Strien, P.M.H., Bindels, E.M., Heckl, D., Büsche, G., Fleck, D., et al. (2017). Gli1+ Mesenchymal Stromal Cells Are a Key Driver of Bone Marrow Fibrosis and an Important Cellular Therapeutic Target. *Cell Stem Cell* 20, 785–800.
- Schubert, M., Klinger, B., Klünemann, M., Sieber, A., Uhlitz, F., Sauer, S., Garnett, M.J., Blüthgen, N., and Saez-Rodriguez, J. (2018). Perturbation-response genes reveal signaling footprints in cancer gene expression. *Nat. Commun.* 9, 20.
- Skene, N.G., and Grant, S.G. (2016). Identification of Vulnerable Cell Types in Major Brain Disorders Using Single Cell Transcriptomes and Expression Weighted Cell Type Enrichment. *Front. Neurosci.* <https://doi.org/10.3389/fnins.2016.00016>.
- Subramanian, A., Tamayo, P., Mootha, V.K., Mukherjee, S., Ebert, B.L., Gillette, M.A., Paulovich, A., Pomeroy, S.L., Golub, T.R., Lander, E.S., and Mesirov, J.P. (2005). Gene set enrichment analysis: a knowledge-based approach for interpreting genome-wide expression profiles. *Proc. Natl. Acad. Sci. USA* 102, 15545–15550.
- Supek, F., Bošnjak, M., Škunca, N., and Šmuc, T. (2011). REVIGO summarizes and visualizes long lists of gene ontology terms. *PLoS ONE* 6, e21800.
- Tikhonova, A.N., Dolgalev, I., Hu, H., Sivaraj, K.K., Hoxha, E., Cuesta-Domínguez, Á., Pinho, S., Akhmetzyanova, I., Gao, J., Witkowski, M., et al. (2019). The bone marrow microenvironment at single-cell resolution. *Nature* 569, 222–228.
- Trapnell, C., Cacchiarelli, D., Grimsby, J., Pokharel, P., Li, S., Morse, M., Lennon, N.J., Livak, K.J., Mikkelsen, T.S., and Rinn, J.L. (2014). The dynamics and regulators of cell fate decisions are revealed by pseudotemporal ordering of single cells. *Nat. Biotechnol.* 32, 381–386.
- Türei, D., Korcsmáros, T., and Saez-Rodriguez, J. (2016). OmniPath: guidelines and gateway for literature-curated signaling pathway resources. *Nat. Methods* 13, 966–967.
- Vainchenker, William, and Plo, Isabelle (2016). EZH2: A Molecular Switch of the MPN Phenotype. *Blood* 127, 3297–3298.
- Vainchenker, W., Delhommeau, F., Constantinescu, S.N., and Bernard, O.A. (2011). New mutations and pathogenesis of myeloproliferative neoplasms. *Blood* 118, 1723–1735.
- Vento-Tormo, R., Efremova, M., Botting, R.A., et al. (2018). Single-cell reconstruction of the early maternal–fetal interface in humans. *Nature* 563, 347–353.
- Vogl, T., Stratis, A., Wixler, V., Völler, T., Thurainayagam, S., Jorch, S.K., Zenker, S., Dreiling, A., Chakraborty, D., Fröhling, M., et al. (2018). Autoinhibitory regulation of S100A8/S100A9 alarmin activity locally restricts sterile inflammation. *J. Clin. Invest.* 128, 1852–1866.
- Wu, H., Gordon, J.A.R., Whitfield, T.W., Tai, P.W.L., van Wijnen, A.J., Stein, J.L., Stein, G.S., and Lian, J.B. (2017). Chromatin dynamics regulate mesenchymal stem cell lineage specification and differentiation to osteogenesis. *Biochim. Biophys. Acta. Gene Regul. Mech.* 1860, 438–449.
- Yamazaki, S., Ema, H., Karlsson, G., Yamaguchi, T., Miyoshi, H., Shioda, S., Taketo, M.M., Karlsson, S., Iwama, A., and Nakauchi, H. (2011). Nonmyelinating Schwann cells maintain hematopoietic stem cell hibernation in the bone marrow niche. *Cell* 147, 1146–1158.
- Yang, Y., Akada, H., Nath, D., Hutchison, R.E., and Mohi, G. (2016). Loss of Ezh2 cooperates with Jak2V617F in the development of myelofibrosis in a mouse model of myeloproliferative neoplasm. *Blood* 127, 3410–3423.
- Yu, G., Wang, L.-G., Han, Y., and He, Q.-Y. (2012). clusterProfiler: an R package for comparing biological themes among gene clusters. *OMICS* 16, 284–287.
- Zambetti, N.A., Ping, Z., Chen, S., Kenswil, K.J.G., Mylona, M.A., Sanders, M.A., Hoogenboezem, R.M., Bindels, E.M.J., Adisty, M.N., Van Strien, P.M.H., et al. (2016). Mesenchymal Inflammation Drives Genotoxic Stress in Hematopoietic Stem Cells and Predicts Disease Evolution in Human Pre-leukemia. *Cell Stem Cell* 19, 613–627.

STAR★METHODS

KEY RESOURCES TABLE

REAGENT or RESOURCE	SOURCE	IDENTIFIER
Antibodies		
BD Pharm Lyse	BD Biosciences	Cat#555899; RRID: AB_2869057
Biotin anti-mouse CD45 Antibody	Biolegend	Cat#103104; RRID: AB_312969
Biotin anti-mouse CD71 Antibody	Biolegend	Cat#113803; RRID: AB_313564
CD41-Biotin	Biolegend	Cat#133930; RRID: AB_2572133
Lineage Cell Depletion Kit, mouse	Miltenyi Biotec	Cat#130-090-858
APC/Cyanine7 anti-mouse CD41 Antibody	Biolegend	Cat#133928; RRID: AB_2572131
APC/Cyanine7 anti-mouse CD3 Antibody	Biolegend	Cat#100222; RRID: AB_2242784
APC/Cyanine7 anti-mouse/human CD11b Antibody	Biolegend	Cat#101226; RRID: AB_830642
APC/Cyanine7 anti-mouse Ly-6G/Ly-6C (Gr-1) Antibody	Biolegend	Cat#108424; RRID: AB_2137485
APC/Cyanine7 anti-mouse TER-119/ Erythroid Cells Antibody	Biolegend	Cat#116223; RRID: AB_2137788
APC/Cyanine7 anti-mouse/human CD45R/ B220 Antibody	Biolegend	Cat#103224; RRID: AB_313007
APC/Cyanine7 anti-mouse CD45.1 Antibody	Biolegend	Cat#110716; RRID: AB_313505
APC/Cyanine7 anti-mouse CD45.2 Antibody	Biolegend	Cat#109824; RRID: AB_830789
PerCP/Cy5.5 anti-mouse Ly-6A/E (Sca-1)	Sony Biotechnologies	Cat#1212615; RRID: AB_2877117
APC anti-mouse CD31 Antibody	Biolegend	Cat#102410; RRID: AB_312905
PE anti-mouse CD51 Antibody	Biolegend	Cat#104106; RRID: AB_2129493
Hoechst Solution 33342	BD Biosciences	Cat#561908
Pacific Blue anti-mouse CD45 Antibody	Biolegend	Cat#103125; RRID: AB_493536
CD11b Monoclonal Antibody (M1/70), eFluor 450	ThermoFisher	Cat#48-0112-80; RRID: AB_1582237
PE/Cy7 anti-mouse CD140a Antibody	Biolegend	Cat#135911; RRID: AB_2715973
APC CD140b (PDGFRB) Monoclonal Antibody (APB5)	ThermoFisher	Cat#14-1402-82; RRID: AB_467493
PE anti-mouse CD106 Antibody	Biolegend	Cat#105713; RRID: AB_1134166
FITC CD107a antibody	BD Biosciences	Cat#553793; RRID: AB_395057
Recombinant Anti-MRP8 antibody [EPR3554]	abcam	Cat#ab92331; RRID: AB_2050283
Rabbit anti-CD56 (clone RCD56, Isotype IgG)	Zytomed Systems	Cat#RBK050; RRID: AB_2864528
APC anti-human CD105 Antibody	Biolegend	Cat#323208; RRID: AB_755960
PE anti-human CD271 (NGFR) Antibody	Biolegend	Cat#345106; RRID: AB_2152647
APC/Cyanine7 anti-human CD31 Antibody	Biolegend	Cat#303120; RRID: AB_10640734
FITC anti-human CD45 Antibody	Biolegend	Cat#368508; RRID: AB_2566368
FITC anti-human CD235ab Antibody	Biolegend	Cat#306610; RRID: AB_756046
FITC anti-human CD71 Antibody	Biolegend	Cat#334104; RRID: AB_2201482
FITC anti-human CD41 Antibody	Biolegend	Cat#303704; RRID: AB_314374
FITC anti-human CD61 Antibody	Biolegend	Cat#336404; RRID: AB_1227580
7-AAD Viability Staining Solution	Biolegend	Cat#420404
goat anti-IL-33 Antibody	R&D Systems	Cat#AF3626; RRID: AB_884269

(Continued on next page)

Continued

REAGENT or RESOURCE	SOURCE	IDENTIFIER
Rabbit anti goat Antibody	DAKO	Cat#E0466
rabbit-anti-S100-Antibody	DAKO	Cat#Z0311
goat anti-rabbit-Antibody	Vector	Cat#BP-9100
Anti-Actin, α -Smooth Muscle - FITC Antibody	Sigma Aldrich	Cat#F3777; RRID: AB_476977
Bacterial and Virus Strains		
pRRL.PPT.SFFV.IRES2.EGFP.WPRE	Axels Schambach, Dirk Heckl	N/A
MSCV-IRES-EGFP	Tannishtha Reya	Addgene Plasmid #20672; RRID:Addgene_20672
pMIG-JAK2WT-IRES-EGFP	Melanie Curie	N/A
pMIG-JAK2V617F-IRES-EGFP	Melanie Curie	N/A
Biological Samples		
Chemicals, Peptides, and Recombinant Proteins		
Murine thrombopoietin	Peprotech	Cat#351-14
Murine stem cell factor	Peprotech	Cat#250-03
Retronectin	Takara Bio	Cat#T100A/B
Polybrene	Merck Millipore	Cat#TR-1003-G
Fugene	Promega	Cat#E2691
StemSpan SFEM	Stem Cell Technologies	Cat#09600
Collagenase II	Invitrogen	Cat#17101015
Murine bFGF	Peprotech	Cat#450-33
Murine EGF	Peprotech	Cat#315-09
Recombinant murine IL-33	Peprotech	Cat#210-33
Recombinant human TGF- β 1	InvivoGen	Cat#rcyc-htgfb1
Poly(ethylene glycol) BioUltra 300	Sigma	Cat#90878-250ML-F
Tasquinimod (ABR-215050)	Biorbyt	Cat#ORB251345
B-27 Supplement (50X), serum free	ThermoFisher	Cat#17504044
Forskolin	Sigma-Aldrich	Cat#F6886
Recombinant Human PDGF-AA	Peprotech	Cat#100-13A
Heregulin- β 3, Epidermal growth factor (EGF) domain	Sigma-Aldrich	Cat#01-201
Liberase	Roche	Cat#5401020001
DNaseI	Sigma	Cat#DN25
Antigen unmasking solution	Vector	Cat#H-3300
Hematoxylin Solution, Gill No. 1	Sigma	Cat#GHS1128
Critical Commercial Assays		
Chromium Single Cell 3' Reagent Kits (v2)	10x Genomics	Cat#PN-120237
Chromium Single Cell A Chip Kit (v2)	10x Genomics	Cat#PN-120236
i7 Multiplex Kit, 96 rxns	10x Genomics	Cat#PN-120262
Single Cell 3' Reagent Kits (v2) User Guide	10x Genomics	Cat#CG00052, Rev D
High-Capacity cDNA Reverse Transcription Kits	Thermo Fisher	Cat#4368814
Fast SYBR Green Master Mix	Applied Biosystems	Cat#4385616
MesenCult Expansion Kit (Mouse)	STEMCELL	Cat#05513
Reticulin silver plating kit acc. to Gordon & Sweets	Sigma	Cat#1002510001
Human S100A8 DuoSet ELISA	R&D Systems	Cat#DY4570-05
Chromium Single Cell 3' Reagent Kits (v2)	10x Genomics	Cat#PN-120237
Chromium Single Cell A Chip Kit (v2)	10x Genomics	Cat#PN-120236

(Continued on next page)

Continued

REAGENT or RESOURCE	SOURCE	IDENTIFIER
i7 Multiplex Kit, 96 rxns	10x Genomics	Cat#PN-120262
Single Cell 3' Reagent Kits (v2) User Guide	10x Genomics	Cat#CG00052, Rev D
AVIDIN/BIOTIN blocking Kit	Vector	Cat#SP-2001
Peroxidase substrate Kit	Vector	Cat#SK-4100
ABC-Kit	Vector	Cat#PK-6100
Deposited Data		
Genome Reference Consortium Mouse Build 38 patch release 6, mm10	Genome Reference Consortium	https://www.ncbi.nlm.nih.gov/assembly/GCF_000001635.26
Raw Data	This paper	GEO: GSE156644
Analyzed Data	This paper	10.5281/zenodo.3979087
Experimental Models: Cell Lines		
Hek293T	ATCC	CRL-3216; RRID:CVCL_0063
Experimental Models: Organisms/Strains		
B6.SJL-Ptpr ^c Pepc ^b /BoyJ <i>Mus musculus</i>	The Jackson Laboratory	Cat#JAX:002014; RRID:IMSR_JAX:002014
C57BL/6J <i>Mus musculus</i>	The Jackson Laboratory	Cat# JAX:000664; RRID:IMSR_JAX:000664
Gli1tm3(re/ERT2)Alj/J	The Jackson Laboratory	Cat#007913
Rosa26tdTomato (i.e., B6-Cg-Gt(ROSA)26Sorttm(CAG-tdTomato)Hze/J)	The Jackson Laboratory	Cat#007909
Oligonucleotides		
See Table S6	See Table S6	See Table S6
Recombinant DNA		
psPAX2 (lentiviral packaging)	Didier Trono	Addgene Plasmid #12259; RRID:Addgene_12259
pCMV-VSV-G (lentiviral envelope)	Didier Trono	Addgene Plasmid #8454; RRID:Addgene_8454
pCL-Eco (retroviral packaging)	Novus Biologicals	Cat# NBP2-29540
Software and Algorithms		
GraphPadPrism v8	GraphPad Software Inc.	RRID:SCR_002798
FlowJo v10	Tree Star Inc.	RRID:SCR_008520
Adobe Phostoshop CC 2018	Adobe Systems Inc.	RRID:SCR_014199
Adobe Illustrator CC 2018	Adobe Systems Inc.	RRID:SCR_010279
Cellranger v 2.1.1	10x Genomics	https://support.10xgenomics.com/single-cell-gene-expression/software/release-notes/2-1
Seurat (v2.3.4; v3.1.0)	Butler et al., 2018	https://satijalab.org/seurat
clusterProfiler v3.12.0	(Yu et al., 2012)	https://git.bioconductor.org/packages/clusterProfiler
edgeR v3.26.7	McCarthy et al., 2012	https://git.bioconductor.org/packages/edgeR
Monocle v2.12.0	Trapnell et al., 2014 Qiu et al., 2017	https://git.bioconductor.org/packages/monocle
R v3.6.1	CRAN	https://www.R-project.org
Progeny v1.11.0	Schubert et al., 2018	https://github.com/saezlab/progeny
Viper v1.20.0	(Alvarez et al., 2016)	https://git.bioconductor.org/packages/viper
CellPhoneDB v2.0.5	Efremova et. al, 2020	https://github.com/Teichlab/cellphonedb
biomaRt v1.2.0	(Durinck et al., 2009)	https://git.bioconductor.org/packages/biomaRt

RESOURCE AVAILABILITY

Lead contact

Further information and requests for resources and reagents should be directed to and will be fulfilled by the Lead Contact, Rebekka K. Schneider, MD, PhD (reschneider@ukaachen.de).

Materials availability

This study did not generate new unique reagents. For specific details on availability please refer to the [Key Resources Table](#).

Data and code availability

Single cell sequencing experiments are deposited at GEO with accession number GEO: GSE156644. Seurat objects of datasets, sample markdown code and tables with complete marker genes, differential expression, gene expression enrichment analysis and ligand receptor analysis are deposited at Zenodo (<https://doi.org/10.5281/zenodo.3979087>).

EXPERIMENTAL MODEL AND SUBJECT DETAILS

Animal studies

All mouse studies were approved by the Animal Welfare/Ethics committee of the EDC in accordance with legislation in the Netherlands (approval No. AVD1010020173387). *Ptprc^aPepc^b*/BoyCr1 (B6.SJL) mice were purchased from Charles River (Netherlands) and maintained in specific-pathogen-free conditions. Mice were maintained on a 12-hr light/dark cycle and were provided with water and standard mouse chow *ad libitum*. Mice were randomly assigned to experimental groups.

Gli1CreERT2 (i.e., Gli1tm3(re/ERT2)Alj/J, JAX Stock #007913), Rosa26tdTomato (i.e., B6-Cg-Gt(ROSA)26Sorttm(CAG-tdTomato)Hze/J JAX Stock #007909) were purchased from Jackson Laboratories (Bar Harbor, ME, USA). Offspring was genotyped by PCR according to the protocol from the Jackson laboratory.

Human studies

For single cell studies from bone marrow biopsies only excess material was used. In accordance with MEC-2018-1445 all patient material was de-identified at inclusion. Unprocessed bone marrow biopsies were obtained approximately 1-2h after successful bone marrow biopsy via the Department of Pathology. More detailed information on patient characteristics can be found in [Figures S7A](#) and [S7C](#).

MPN Patient plasma samples were collected and supplied by the University Clinic Hamburg-Eppendorf (UKE), obtained via the German Study Group MPN Aachen and the Department for Molecular Diagnostics at the Erasmus Medical Center (MC) in Rotterdam. Control samples were obtained via the Institute for Clinical Chemistry at Erasmus MC. Surplus material was collected from dermatological, and cardiological, orthopedic or neurological patients after diagnostics according to the ethical vote MEC-2018-1445 and processed on the day of acquisition. All subjects had no history or indication of any hematological or non-hematological malignancy. Samples were de-identified at the time of inclusion. All patients provided informed consent and the data collection was performed in accordance with the Declaration of Helsinki.

For samples from Bern all patients and healthy donors gave written informed consent and all analyses of the samples were approved by the Cantonal Ethics Committee of Bern (2016-01949). Human bone marrow tissues were provided by the Tissue Bank Bern.

Human bone marrow biopsies from a subcohort of patients whose plasma was used were chosen for histological examination from archived patient samples of paraffin-embedded tissue from the Biobank of Dr. G. Büsche at the Department of Pathology, Hannover Medical School, Hannover, Germany. Biopsies were primarily taken during earlier hospitalization. Additional control bone marrow slides were acquired from the Department of Pathology at Erasmus Medical Center. All reference patients showed normal bone marrow characteristics and had no evidence for a history of hematological malignancies.

Cell lines and cell culture

For MSC isolation, bones of WT mice were crushed and digested with Collagenase II (Invitrogen, #17101015) for 90 min at 37°C. Bone chips were washed three times with alpha-MEM/ 10% FCS/ 1% Penicillin/Streptomycin, transferred to a 15cm culture dish and cultured in full medium (alpha-MEM, 10% FCS, 1% Penicillin/Streptomycin, 1ng/ml murine bFGF (Peprotech, #450-33), 5ng/ml murine EGF (Peprotech #315-09)). After 72h bone chips were transferred to a new culture dish to dispose of contaminating macrophages. After 7–9 days, the bone chips were discarded. Attached MSCs were washed, trypsinated, centrifuged, and replated. Cells were passaged every 2-4 days at approximately 80% confluence.

METHOD DETAILS

Viral transduction

For retroviral and lentiviral transduction, c-kit⁺-enriched cells from 8-12-week-old WT mice were isolated by crushing compact bone and lineage depleted by magnetic separation (Miltenyi Biotec). c-kit⁺ BM cells were pre-stimulated for 24 h in CellGro media (Cell-Genix) supplemented by murine stem-cell factor (m-Scf., 50ng/ml, Peprotech) and murine thrombopoietin (m-Tpo, 50ng/ml, Peprotech). Oncoretroviral vectors were pseudotyped with an Ecotropic Envelope Vector and produced using standard protocols.

Retroviral transduction was performed on retroNectin (Takara Bio)-coated cell culture dishes loaded with unconcentrated virus. Cells were resuspended in medium containing concentrated virus in the presence of 4 µg/ml polybrene at 37°C for a minimum of 24 h.

Lentiviral particles were produced by transient transfection with lentiviral plasmid together with pSPAX and VSVG packaging plasmids using Fugene (Promega). Lentiviral and retroviral particles were concentrated by ultracentrifugation at 4°C.

Induction of myelofibrosis by overexpression of ThPO or JAK2^{V617F}

8-10-week-old female B6.SJL recipients mice were irradiated with 10.5 Gy and received 4-5x10⁵ cells from 8-week-old WT littermates that had been harvested 48 h prior to transplantation and transduced with ThPO (GFP⁺) lentivirus or control empty vector lentivirus (Empty Vector-GFP⁺). For JAK2^{V617F} studies (JAK2), WT BM cells were transduced with JAK2^{V617F} retrovirus or control pMIG retrovirus (control: JAK2 empty vector).

Mice from the early ThPO cohort were sacrificed 5 weeks post-transplant and mice in the late ThPO cohort were sacrificed 10 weeks post-transplant. Mice used in the JAK2 experiments were sacrificed at 26 weeks post-BM transplant. Mice in the JAK2 and ThPO late cohort were sacrificed when they had signs of advanced fibrosis as indicated by dropping hemoglobin levels and apparent weight loss.

Blood was periodically collected from mice via submandibular bleeds into Microtainer tubes coated with K₂EDTA (Becton Dickinson, NJ, USA) and complete blood counts were performed on a Horiba Scil Vet abc Plus hematology system.

For the quantification of MSC-1/2 and MSC-3/4 in ThPO-setting, 6-10 week old B6.Cg-Tg(Grem1-cre/ERT)3Tcw/J recipient mice were injected 4x30mg with tamoxifen in corn oil/ 3% ethanol (Sigma) intraperitoneally. Three weeks after last tamoxifen injection, mice were irradiated using a split-scheme of 2 × 6.02Gy and received 4-5x10⁵ cells from 8-week-old littermates that had been harvested 48 h prior to transplantation and transduced with ThPO (GFP⁺) lentivirus or control empty vector lentivirus (Empty Vector-GFP⁺).

Isolation of bone marrow stromal cells for scRNA sequencing

After sacrifice bones (femurs, hip, spine) were crushed and flushed in PBS/2% FCS on ice. The cells were dissociated by filtering through a 70µm nylon mesh. Cells were lineage depleted using biotinylated antibodies directed against lineages (CD5, CD45R (B220), CD11b, Anti-Gr-1 (Ly-6G/C), 7-4 and Ter-119) (Miltenyi Biotec) and CD45, CD71 and CD41 (Biolegend). The cells were stained for 10 min at 4°C. After washing, the cells were incubated with anti-biotin beads (Miltenyi biotec) for 15 min at 4°C prior to magnetic depletion using a cell separation magnet (BD). The cells that were not bound to the magnet were used for FACS staining and sorting.

Human biopsies were crushed and flushed with PBS/10% FCS on ice and filtered through a 70µm nylon mesh. Cleaned bone chips were digested in 10ml collagenase II (1mg/ml) at 37°C for 90 min under gentle agitation. The cell suspension was strained through a 70µm mesh and bone chips were additionally washed twice with PBS/10% FCS before pooling it with the flushed fraction. Both fractions were used for FACS staining and sorting.

FACS-staining and sorting of bone marrow stromal cells for scRNA sequencing

Cells were resuspended in 300µl PBS/2% FCS and stained at 4°C for 20 min with the antibodies described below. Washing was performed by adding 1ml PBS/2% FCS and centrifuging for 5 min at 300 × g, 4°C. After resuspension and addition of Hoechst (1:10000), lineage/CD45/Ter119 negative cells were sorted into 50µl DMEM/10% FCS (BD Aria III) and used for the 10x platform. Unstained cells were used as negative controls to define gating. All antibodies were acquired from Biolegend.

The following fluorochrome conjugated antibodies were used for murine samples: CD41-APC-Cy7, CD3-APC-Cy7, CD11b-APC-Cy7, Gr1-APC-Cy7, Ter119-APC-Cy7, B220-APC-Cy7, CD45.1-APC-Cy7, CD45.2-APC-Cy7, Sca1-PerCP, CD31-APC, CD51-PE.

Patient derived cells were stained following the same protocol using the following conjugated antibodies: CD105-APC, CD271-PE, CD31-APC-Cy7, CD45-FITC, CD235a-FITC, CD71-FITC, CD41-FITC, CD61-FITC

Isolation of Gli1⁺ stromal cells in homeostasis for scRNAseq

For lineage tracing, 6-7 week old mice were injected intraperitoneally with 4x3 mg tamoxifen in corn oil / 3% ethanol (Sigma). Mice were sacrificed 2 weeks after the last injection of tamoxifen. At sacrifice, compact bones were crushed and flushed in PBS/2% FCS and dispersed into a single cell suspension prior to red blood cell lysis to obtain the bone marrow fraction. Bone chips were digested with Liberase (0.2mg/ml; 5401020001, Roche) in the presence of DNase I (60Units/mL, DN25-100MG) for 30 min at 37°C with agitation. The cell suspension was then filtered through a 70µm nylon mesh and combined with the bone marrow fraction before addition of Hoechst (1:10000). Viable Gli1-tdTom⁺ cells were sorted (BD Aria II) into DMEM/10% FCS and used for the 10x platform.

Single cell library preparation and sequencing

The libraries were prepared using the Chromium Single Cell 3' Reagent Kits (v2): Single Cell 3' Library & Gel Bead Kit v2 (PN-120237), Chromium Single Cell A Chip Kit v2 (PN-120236) and i7 Multiplex Kit (PN-120262) (10x Genomics), and following the Single Cell 3' Reagent Kits (v2) User Guide (manual part no. CG00052, Rev D). Finalized libraries were sequenced on a Novaseq6000 platform (Illumina), aiming for a minimum of 50,000 reads/cell using the 10x Genomics recommended number of cycles (28-8-0-91 cycles).

Single cell RNA seq data analysis of ThPO and Jak2 mouse models

We used cellranger (version 2.1.1) to align reads to mouse genome mm10 and for detection of cells with default parameters. Next, we used Seurat (v3.1.0) for high level analysis of the scRNA-seq (Satija et al., 2015). We filtered cells with a high amount of mitochondrial

genes (< 0.1), high amount of ribosomal genes (< 0.25). We also removed cells with more than 30,000 UMIs as they represent potential multiplets. Finally, we filtered cells with less than 30 genes detected. See [Table S1](#) for quality statistics of RNA-seq libraries.

Next, we regressed out cell cycle, the proportion of mitochondrial, ribosomal and UMI counts and performed a log-normalization of read counts using Seurat for data. Next, samples from ThPO (and Jak2) experiments were integrated with canonical correlation analysis (CCA) based on the first 15 CCs ([Butler et al., 2018](#)). Unsupervised clustering was performed selecting $k = 15$ with a shared nearest neighbors graph with resolution 0.8. UMAP representations were generated using the following parameters: $\text{min_dist} = 0.3$, $\text{max_dim} = 2$, $\text{seed.use} = 36$). We used FindMarkers gene function with adjusted p value < 0.05 to find cluster specific makers.

Differential gene expression analysis was performed with Seurat changing between distinct phenotypes. For this, we considered only genes with an absolute fold change greater than 0.5 and adjusted p value < 0.01. GO and pathway enrichment analysis were based on clusterProfiler (Version 3.12.0; [Yu et al., 2012](#)) and CAMERA from edgeR (Version 3.26.7; ([McCarthy, Chen and Smyth, 2012](#))). Obtained GO terms were summarized via the REVIGO web application using p values as input metric allowing a similarity of 0.7 ([Supek et al., 2011](#)). We have also defined gene sets describing “hematopoiesis-support,” “MSC progenitor phenotype,” “non-collagenous ECM” and “collagenous ECM” ([Table S2](#)). These were used in a pre-ranked GSEA analysis (Version 4.0; ([Subramanian et al., 2005](#))). All p values were corrected by Benjamini-Hochberg correction. A full list of identified marker genes and differentially expressed genes for each dataset including corresponding statistics is supplied in [Tables S2](#) and [S3](#).

Integration of single cell RNA seq data of Gli1 sorted cells

We used the previously described computational pipeline for analysis of Gli1 sorted scRNA-seq cells. We filter cells by fraction of mitochondrial genes (< 0.1), low amount of ribosomal genes (< 0.08) or cells with less than 200 genes detected. The Gli1 data were integrated with the ThPO data using a label transfer procedure from Seurat (v3.1.0). This allowed us to associate Gli1 cells to the 7 clusters detected in ThPO cells.

Single cell RNA seq data analysis of human samples

We used the previously described computational pipeline for normalization and integration of human samples. Reads were aligned to the genome GRCh38 and we filtered cells with high fraction of mitochondrial genes (< 0.2), high fraction of ribosomal genes (< 0.4) and lower number of UMIs (> 45). Also, cells with less than 200 genes detected and cells with more than 12,000 UMIs were removed. Integration, clustering analysis was performed by Seurat (v3.1.0) as described before.

Reconstructing cell development trajectories

We used monocle (version 2.12.0, ([Trapnell et al., 2014](#))) to reconstruct the cell development trajectories by combining all mouse data (ThPO, Jak2 and Gli1 cells) with default parameters. We used the 1000 most relevant genes identified by Monocle’s unsupervised feature selection approach (dpFeature) for the cell development trajectories reconstructing. Next, we used the Branched expression analysis modeling (BEAM, version 2.12.0, ([Qiu et al., 2017](#))) to find genes with branch specific expression patterns. Only genes with an adjusted p value < 0.05 were further considered.

PROGENy analysis

PROGENy analysis was conducted as described using the Progeny package (R, V1.11.0) for human and murine datasets. Reference Progeny papers for each interrogated cluster the generated list of genes differentially expressed between fibrotic and non-fibrotic conditions was used. The scala products of obtained log2-fold changes and PROGENy weights were calculated for respective pathway scores. To estimate significance label permutation was performed 10000 times to generate a Null distribution for each pathway. The pathway scores were scaled to their respective Null distribution to generate a normalized pathway score.

Ligand-receptor analysis

For ligand-receptor analysis we used the CellPhoneDB (Version 2.0.5) tool with some modifications ([Vento-Tormo et al., 2018](#)); [Efronova et al., 2020](#)). Aiming to increase the amount of ligand-receptor pairs available, the original database was extended by OmniPath interactions which are publicly available (https://github.com/saezlab/cellphonedb_omnipath; [Türei et al., 2016](#); ([Ceccarelli et al., 2020](#))). We used log-normalized and scaled scRNA-seq matrices as input. Gene IDs were converted to ENSEMBL IDs using biomaRt (Version 1.2.0; ([Durinck et al., 2009](#))) and EWCE (Version 0.99.2; ([Skene and Grant, 2016](#))). Each data expression table was split based on the respective conditions (experiment versus control for murine datasets and MF versus control for the human dataset). Then, CellPhoneDB was executed for each dataset using the ‘statistical_analysis’. CPDB results were used to build Ligand Receptor networks. We only considered ligand receptor pairs which are expressed in at least 10% of cells of the corresponding cluster in mouse data. Due to the sparsity of the data and the presence of interactions specific to either the fibrotic or the non-fibrotic bone marrow, unfiltered LR lists were considered for human data. Only statistically significant interactions (p value < 0.05) were considered for further analyses. For network plots the expression differences for all inferred ligands and all inferred receptors were averaged for each pair of cell clusters. For individual LR interactions the difference in mean expression between fibrotic and non-fibrotic condition was calculated as described below. Next, we ranked the individual receptor (or ligands) by their number of interactions and normalized them to the number of all possible cell-cell interactions to identify the most influential receptor (ligand) regarding all conditions. For an exhaustive list of ligand-receptor pairs with corresponding statistics, refer to [Table S5](#).

Quantification of S100A8 in human plasma samples

Plasma was isolated from whole blood anticoagulated with EDTA by centrifugation (2000 × g, 7 min) and stored at –80°C. Samples were thawed gently on ice and centrifuged for 5 min at 2500 × g before further processing. Samples were diluted 1:50 - 1:150 and S100A8 concentration was quantified using the Human S100A8 DuoSet ELISA (R&D Systems, DY4570-05) according to the manufacturer's instructions. For each run samples with values outside of the respective standard curve were adjusted to the highest or lowest reliably measurable standard respectively.

Histological and immunohistological analysis

Murine organs were fixed in 4% paraformaldehyde for 24 h and transferred to 70% ethanol. Spleens were weighed before fixation. Femurs were decalcified in 10% EDTA/Tris-HCl (pH 6.6) solution for 72 h, dehydrated, and paraffin embedded. H&E and reticulin staining were performed on 4 μm sections according to established routine protocols.

Human bone marrow biopsies were fixed for 24 h using the Hannover Solution (12% buffered formaldehyde plus 64% methanol), decalcified (EDTA), dehydrated and embedded in paraffin. For the patients, whose material was used for scRNAseq, fixed and stained diagnostic slides were obtained via the Department of Pathology at Erasmus MC.

For immunohistochemical analysis of S100A8 and NCAM1 (CD56), antigen retrieval was performed using citrate-buffer in a conventional lab microwave (Vector, antigen unmasking solution). Sections were treated with 3% H₂O₂ and blocked with Avidin/Biotin blocking kit (Vector), and subsequently incubated with primary antibody (rabbit-anti-S100A8: ab92231, Abcam, 1:200; rabbit-anti-CD56: RBK050, Zytomed Systems, 1:100) for 1 h at room temperature. Biotinylated monoclonal goat anti-rabbit-antibody (Vector) was used as a secondary antibody for 30 min at room temperature. Slides were incubated with AB complex for 30 min at room temperature, washed, and incubated for a further 10 min with DAB substrate. Slides were counterstained with hematoxylin and mounted with glass coverslip using DPX mountant (Sigma).

Immunohistochemical stainings for S100b were performed with an automated, validated, and accredited staining system (Ventana Benchmark ULTRA, Ventana Medical Systems, Tucson, AZ, USA) using optiview universal DAB detection Kit (#760-700). In brief, following deparaffinization and heat-induced antigen retrieval the tissue samples were incubated with rabbit-anti-S100-antibody (DAKO) diluted 1:6000 for 16 min at 36°C. Incubation was followed by hematoxylin II counter-stain for 12 min and then a blue coloring reagent for 8 min according to the manufacturer's instructions (Ventana).

Slides were scanned and digitized in an automated fashion using a Hamamatsu Nanozoomer 2.0 HT system. Images were analyzed and exported using the NDP.view software (Hamamatsu, V2.5.19).

Co-staining of human bone marrow samples for S100b/IL-33

Double immunostaining was performed by automated staining using a Bond RX immunostainer (Leica Biosystems). In brief, all slides were dewaxed in Bond dewax solution (#AR9222, Leica Biosystems). Heat-induced epitope retrieval was done at pH 9 in Tris buffer (#AR9640, Leica Biosystems) for 30 min. at 95°C. The primary antibodies were incubated sequentially. In a first step, goat anti-IL-33 antibody (#AF3626, R&D Systems) was diluted 1:400, incubated for 30 min, and a rabbit anti-goat antibody (#E0466, Dako) was used at a 1:400 dilution for 15 min as secondary antibody. All samples were subsequently incubated with horseradish peroxidase (HRP)-polymer for 15 min. and thereafter visualized using 3,3'-Diaminobenzidine (DAB) as brown chromogen (#DS9800, bond polymer refine detection, Leica Biosystems) for 10 min. In a second step, a rabbit anti-S100 antibody (#Z0311, Dako) was diluted 1:6000 and incubated for 30 min. This antibody was detected using a kit solution containing a polymeric alkaline phosphatase (AP)- linker antibody conjugate system (for 15 min.) and visualized using fast red as red chromogen (#DS9390, red polymer refine detection, Leica Biosystems). Finally, the samples were counter-stained with Haematoxylin and mounted with Aquatex (#108562, Merck).

FACS-staining and sorting of MSC-1/2 and MSC-3/4 for functional analysis

Primary murine stromal cells were used at passage 1. The following fluorochrome conjugated antibodies were used: CD45-ef450 (BioLegend, 103125), CD11b-ef450 (ThermoFisher, 48-0112-80), CD140a-PE-Cy7 (BioLegend, 135911), CD140b-APC (ThermoFisher, 17-1402-82), CD106(VCAM-1)-PE (BioLegend, 105713), Lamp-1-FITC (BD PharMingen, 553793), CD63-APC-Cy7 (BioLegend), and Hoechst 33342 (BD PharMingen, 561908) for live staining. Cells were sorted from the singlet alive CD45neg CD11bneg gate. MSC 1+2 was sorted as: CD140a⁺/CD140b⁺/VCAM-1⁺/CD63⁺/Lamp-1⁺. MSC 3+4 were sorted as: 1) CD140a⁺/CD140b⁺/VCAM-1⁺/CD63⁻/Lamp-1⁻, and as 2) CD140a⁻/CD140b⁻/VCAM-1⁺. Cells were either seeded directly for CFU-F assay or expanded in culture.

CFU-F assay

1,000 sort-purified primary cells were seeded per well in a 6-well adherent tissue culture plate using MesenCult Expansion Kit (STEMCELL Technologies), in the presence of MesenPure (STEMCELL Technologies), and 0.5% penicillin-streptomycin. On day 15, cells were stained with Giemsa (Merck) according to standard protocol and colonies were counted manually.

Growth curve

Sorted cells were cultured in alpha-MEM, 10% FCS, 1% Penicillin/Streptomycin, 1ng/ml murine bFGF (Peprotech, #450-33), 5ng/ml murine EGF (Peprotech #315-09) in a 6-well plate. Twice a week cells were counted and replated in the same concentration (20.000 cells/well).

Recombinant cytokine stimulation of primary murine stromal cells

For recombinant cytokine stimulation, primary stromal cells were seeded at 40,000 cells/well in a 6-well plate and stimulated with recombinant human TGF- β (10ng/ml, Invivogen) for 72 h. Cells were harvested using TriZol (ThermoFisher) and processed for RNA extraction. 500ng of total RNA was reversely transcribed using the high-capacity cDNA Reverse Transcription kit (Applied Biosystems). Quantitative polymerase chain reactions were performed with SYBRGreen PCR master mix (ThermoFisher) on an Applied Biosystems 7500 Real-Time PCR System. Glyceraldehyde-3-phosphate dehydrogenase (*Gapdh*) was used as a housekeeping gene. Differences in RNA levels were calculated using the $2^{-\Delta\Delta CT}$ method. Primer sequences can be found in the [Key Resources Table](#).

MSC to SCP transition

Harvested MSCs were cultured in glutamine-free α -MEM (Sigma) containing 15% FCS.

MSCs at passage 8 were seeded at 100,000 cells/mL in 1:1 (v/v) DMEM/F12 and Neurobasal medium (Invitrogen) with basic fibroblast growth factor (bFGF; 40 ng/mL; Peprotech), epidermal growth factor (20 ng/mL; Peprotech), and B27 (2%, v/v, Invitrogen) in ultra-low-attachment poly(2-hydroxyethyl methacrylate)-coated culture plates (Corning). Medium was replenished every two days. This non-adherent fraction was maintained until the neurospheres reached the size of 80-120 μ m. The neurospheres were seeded onto poly-L-lysine/laminin-coated culture dishes with a density of 8-10 spheres/cm². Cultures were maintained in glutamine-free α -MEM (Sigma) containing 10% FCS and glia inducing factors including forskolin (5 μ M; Sigma), platelet-derived growth factor (PDGF)-AA (5 ng/mL; Peprotech), bFGF (10 ng/mL; Peprotech), and β -heregulin (200 ng/mL; Millipore) for 10 days. Medium was refreshed every 3 days.

Treatment of mice with Tasquinimod

WT recipient mice (n = 7-10/group) were lethally irradiated (10.5Gy) and transplanted with c-kit⁺ HSPCs that were retrovirally transduced with either JAK2^{V617F}- or JAK2^{WT} as described above. Tasquinimod treatment (ABR-215050, Biorbyt) was administered via drinking water at 30mg/kg/day dissolved in 3% sucrose in autoclaved water. Tasquinimod was first dissolved in DMSO, then mixed with 3% sucrose, 2% PEG300 (Sigma) in water. Vehicle-treated groups received DMSO-, PEG300-treated water with 3% sucrose. Drinking bottles were renewed twice a week. Treatment was started at 5 weeks post-transplant until 10 weeks post-transplant and resumed at 13 weeks post-transplant until sacrifice.

Treatment of cells with Tasquinimod

For *in vitro* studies using Tasquinimod, 20,000 Gli1⁺ tdTom⁺ stromal cells were seeded per well in a 6-well plate, in aMEM supplemented by 20% FCS, 1ng/ml bFGF (Peprotech, #450-33), 5 ng/ml murine EGF (Peprotech #315-09). At 24 and 48 h after seeding, cells were treated with recombinant TGF- β (10ng/ml, Invivogen) or PBS control, followed by Tasquinimod treatment (50uM) or DMSO control. For confocal imaging of *in vitro* Tasquinimod experiments, Gli1⁺ tdTom⁺ stromal cells (20,000 cells/well in 6-well plate) were cultured on glass coverslips and treated as described above. At 72 h post-seeding, cells were fixed in 4% paraformaldehyde for 10 min at room temperature. Cells were stained with mouse primary antibody α SMA-FITC (1:100, Sigma, F3777), counterstained with DAPI (4',6'-diamidino-2-phenylindole) and mounted in Prolong Diamond. Images were obtained by confocal microscopy on a Leica SP8 microscope.

Image processing

All plots were generated with GraphPad Prism Version 8.0 or R Version 3.6.1. To ensure readability line thickness, labels and font size were adjusted manually using Adobe Illustrator CC 2018. For joint plotting only identically scaled graphs were used. Unless otherwise specified, images were representatively chosen and jointly rescaled, before manual alignment if necessary.

QUANTIFICATION AND STATISTICAL ANALYSIS

Statistical analysis - excluding that for single cell RNaseq data - was conducted using either GraphPad Prism Version 8.0 or R Version 3.6.1. Unless otherwise specified, data are presented as mean \pm SEM. Two independent groups with (approximately) normally distributed samples were compared with an unpaired t test. When normality could not be assumed, Wilcoxon Rank Sum test was used. For ≥ 2 groups and continuous response variables, ANOVA was employed with post hoc paired t test and Holm-Bonferroni correction for multiple hypothesis testing. For ≥ 2 groups and discrete/ordinal response variables, Kruskal-Wallis H test with post hoc pairwise Wilcoxon Rank Sum test was performed.

For trend analysis the Jonckheere-Terpstra-test was employed. p values were calculated for each researcher independently and corrected for multiple hypothesis testing by the Benjamini-Hochberg procedure.

p values lower or equal to 0.05 were considered statistically significant. Significance is depicted throughout the manuscript as follows: p \leq 0.05: *; p \leq 0.01: **; p \leq 0.0001: ***.

Supplemental Information

Heterogeneous bone-marrow stromal progenitors drive myelofibrosis via a druggable alarmin axis

Nils B. Leimkühler, Hélène F.E. Gleitz, Li Ronghui, Inge A.M. Snoeren, Stijn N.R. Fuchs, James S. Nagai, Bella Banjanin, King H. Lam, Thomas Vogl, Christoph Kuppe, Ursula S.A. Stalmann, Guntram Büsche, Hans Kreipe, Ines Gütgemann, Philippe Krebs, Yara Banz, Peter Boor, Evelyn Wing-Yin Tai, Tim H. Brümmendorf, Steffen Koschmieder, Martina Crysandt, Eric Bindels, Rafael Kramann, Ivan G. Costa, and Rebekka K. Schneider

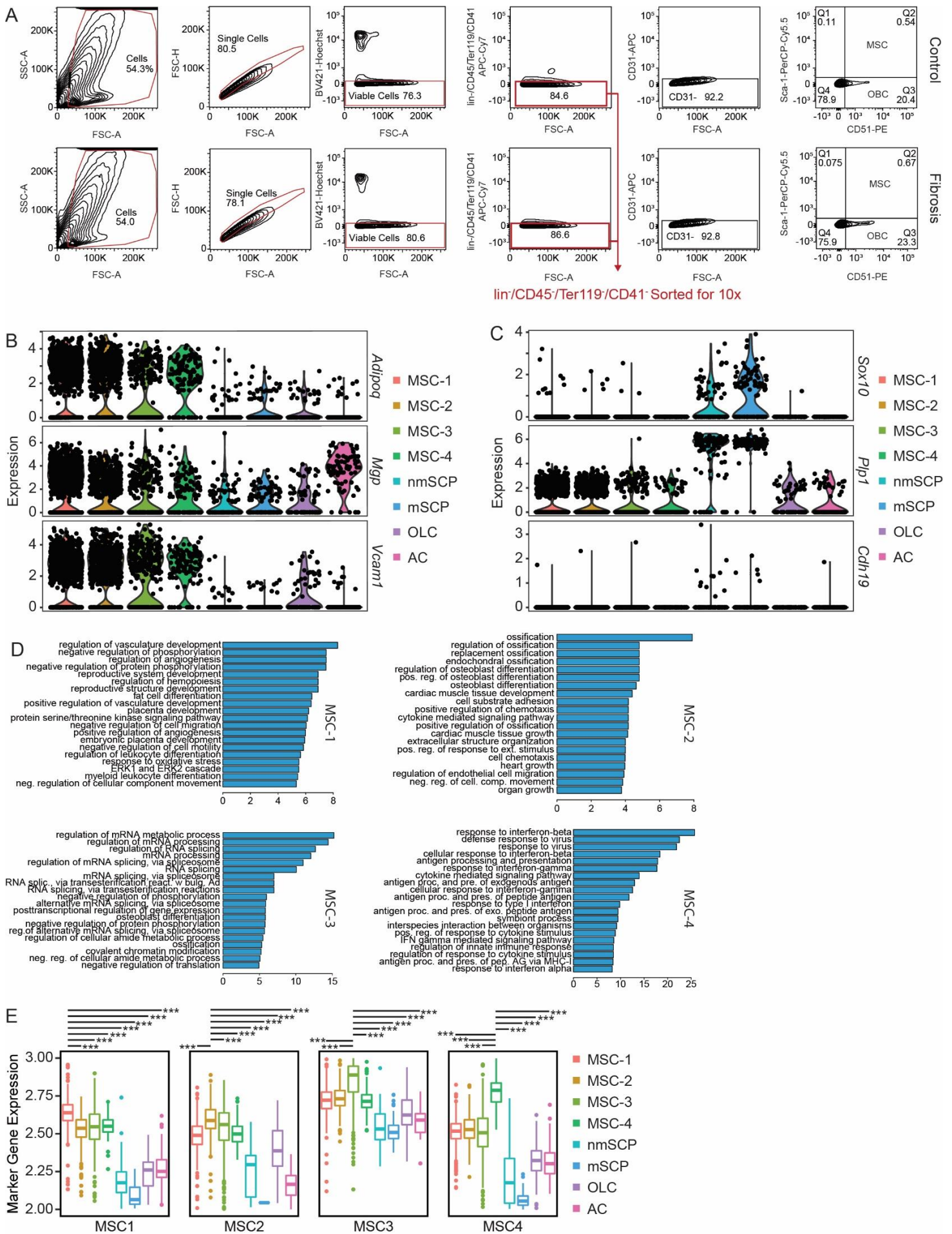


Figure S1: Sorting of non-hematopoietic cells and annotation of identified populations (related to Figure 1 and Table S2)

(A) Sorting strategy for non-hematopoietic cells. After exclusion of multiplets and dead cells, lin-CD45-Ter119-CD41- cells were sorted for scRNAseq. Staining for known niche markers (CD31-APC, CD51-PE, Sca-1-PerCP) were used as quality control. **(B)** Top GO terms corresponding to marker genes identified for the four different MSC-subclusters. GO enrichment analysis was based on clusterProfiler (Version 3.12.0). Significance is given as $-\log(p)$. **(C) (D)** Violin-plots showing the gene expression of respective marker genes per cluster of **(C)** MSCs and **(D)** SCPs. **(E)** Boxplot depicting the aggregated gene expression of respective MSC cluster marker genes in each cell population. Significance was calculated by One-Way-Anova and post-hoc pairwise t-test. The interrogated marker geneset was considered as the respective control for comparisons. p-values were adjusted according to the Benjamini-Hochberg procedure.

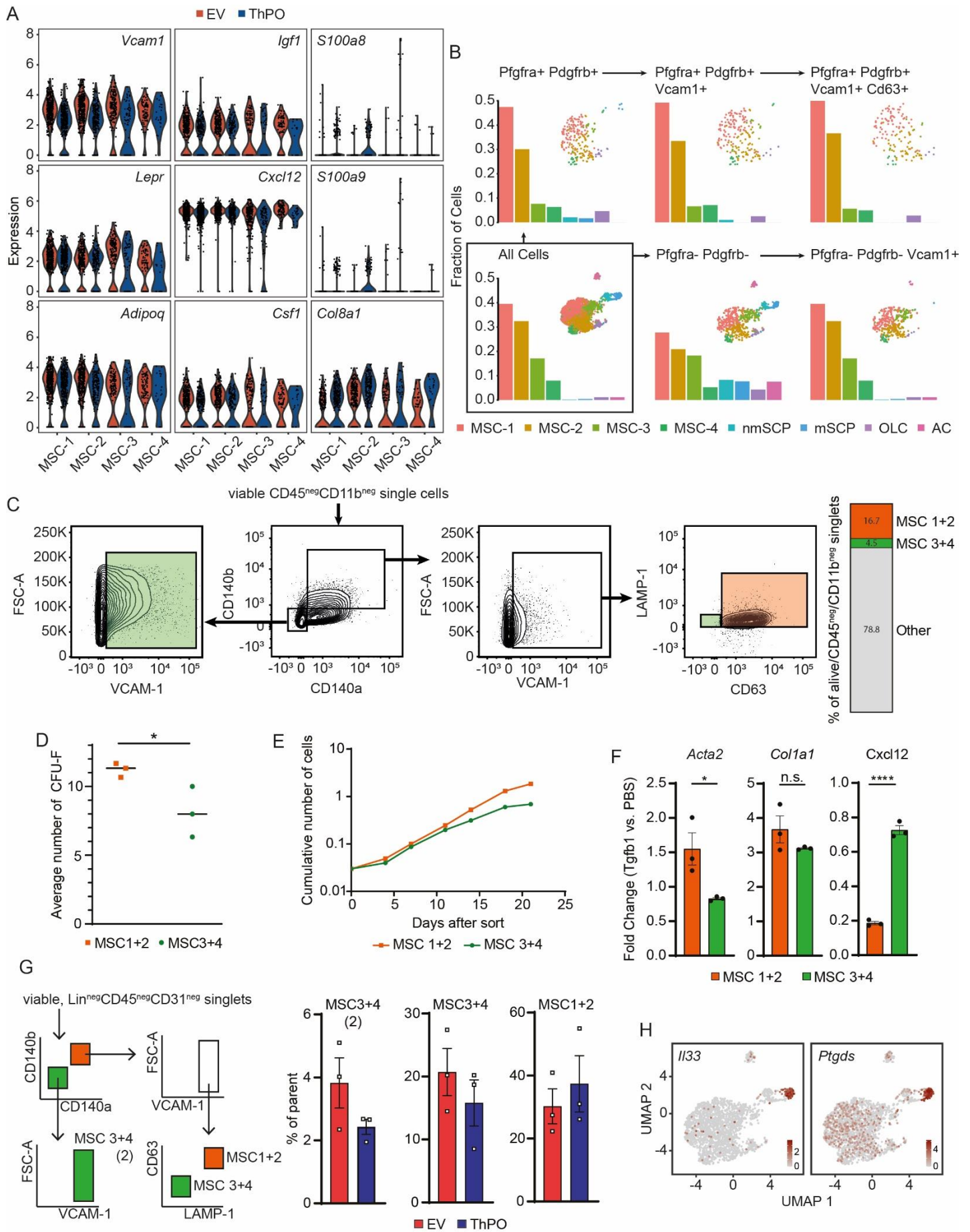


Figure S2: Changes in gene expression between ThPO/EV and functional characterization of MSC-1 and MSC-2 (related to Figure 2 and Table S3, S6)

(A) Violin-plots depicting the expression of respective differentially expressed genes as shown in Figure 2C. Expression levels in non-fibrotic (EV, red) and fibrotic conditions (ThPO, blue) are shown side by side. **(B)** Iterative

subsetting of the entire ThPO dataset on cells expressing relevant surface marker genes as previously described and found to be discriminating in the data shown. The barplot depicts the frequency of each cluster population in the respective subset. The corresponding UMAP of the subsets is depicted in the top right corner of each panel. **(C)** Sorting strategy of primary murine stromal cells. Cells were isolated from the bone chips of two wildtype mice by attachment selection. MSC-1/2 (orange) and MSC-3/4 (green) were sorted as shown. Composition of viable CD45⁻/CD11b⁻ cells is shown as stacked barplot on the right. **(D)** MSC-1/2 and MSC-3/4 were sorted as shown in (C) and immediately plated out in triplicate for the MesenCult colony assay. Colonies were counted by three independent investigators. The average count across all investigators is depicted for each replicate, black lines correspond to the mean across replicates. Significance was calculated by unpaired t-test ($p = 0.0474$). **(E)** Growth curve of sorted MSC-1/2 (orange) and MSC-3/4 (green) populations over time. **(F)** MSC-1/2 and MSC-3/4 were stimulated in triplicate with recombinant Tgf-b1 or PBS as control for 72 hours. qt-PCR was performed for *Acta2* (α -SMA), *Col1a1* and *Cxcl12*. $2^{-\Delta\Delta ct}$ -values were normalized to the respective PBS control. Values are shown as mean \pm SEM. Significance was calculated by unpaired t-test. **(G)** Bone marrow of non-fibrotic (EV, red) and fibrotic mice (ThPO, blue) was harvested at week 7.5 post transplantation. MSC-1/2 and MSC-3/4 were isolated from lineage depleted bone marrow as shown in the left panel. Values are shown as mean \pm SEM. Significance was calculated by unpaired t-test. **(H)** Expression of Interleukin-33 (*Il33*) and Prostaglandin-H2 D-isomerase (*Ptgds*) projected onto the UMAP space of isolated cells.

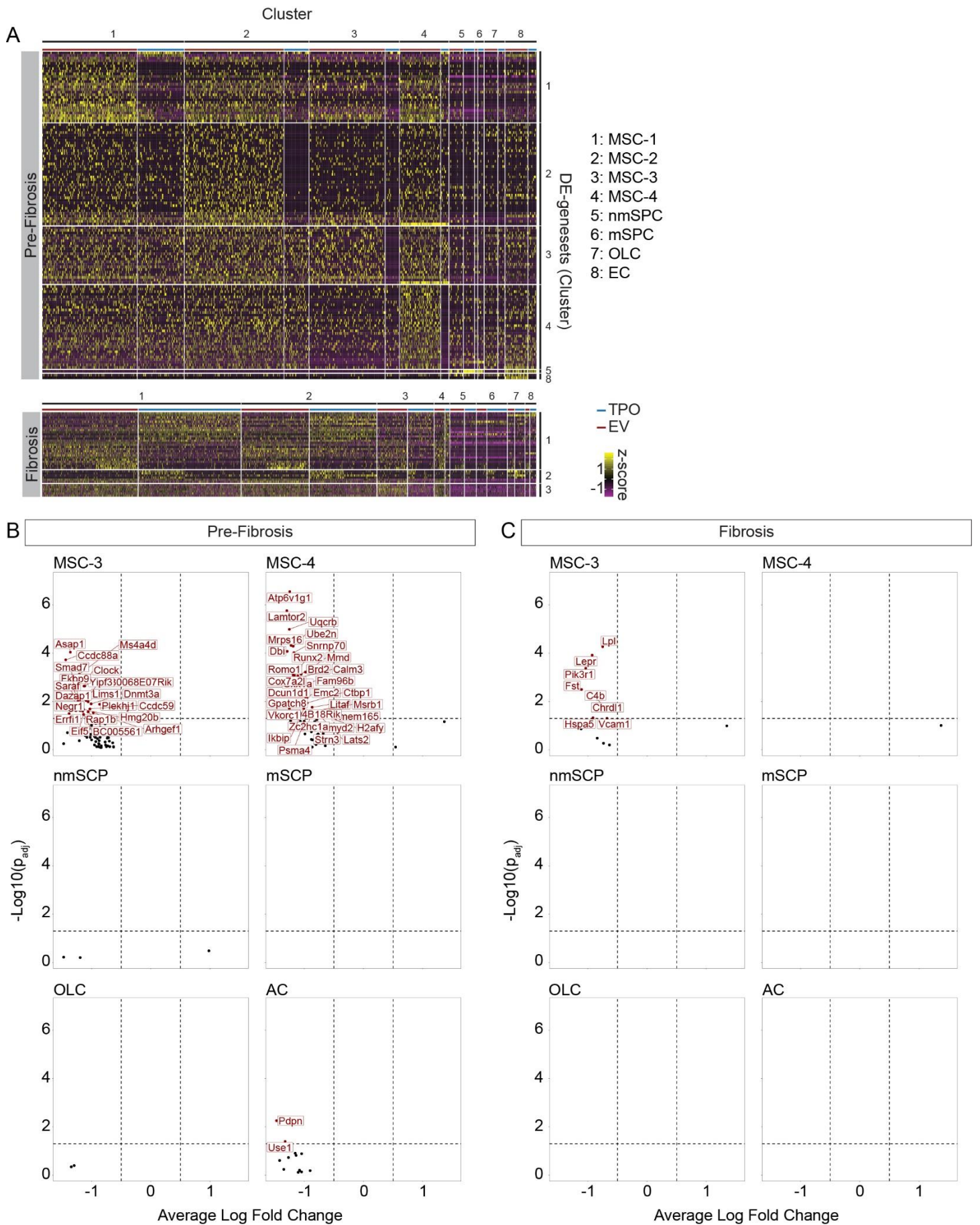


Figure S3: Differential gene expression in different clusters at different timepoints (related to Figure 3 and Table S3)

(A) Heatmap depicting differentially expressed genes between TPO and EV for all clusters. For each cluster expression of identified DE genes is shown under experimental (TPO, blue) and control conditions (EV, red). DE-genesets contain all differentially expressed genes of indicated clusters. The clusters for which genesets the expression is shown are indicated

on the right. **(B-C)** Volcano plot of differentially expressed genes (Wilcoxon rank sum test, two tailed; calculated per cluster individually) between TPO and EV for MSC-3, MSC-4 and non-MSC clusters. Data are shown for **(B)** Pre-Fibrosis (TPO, 4 weeks) and **(C)** Fibrosis (TPO, 8 weeks).

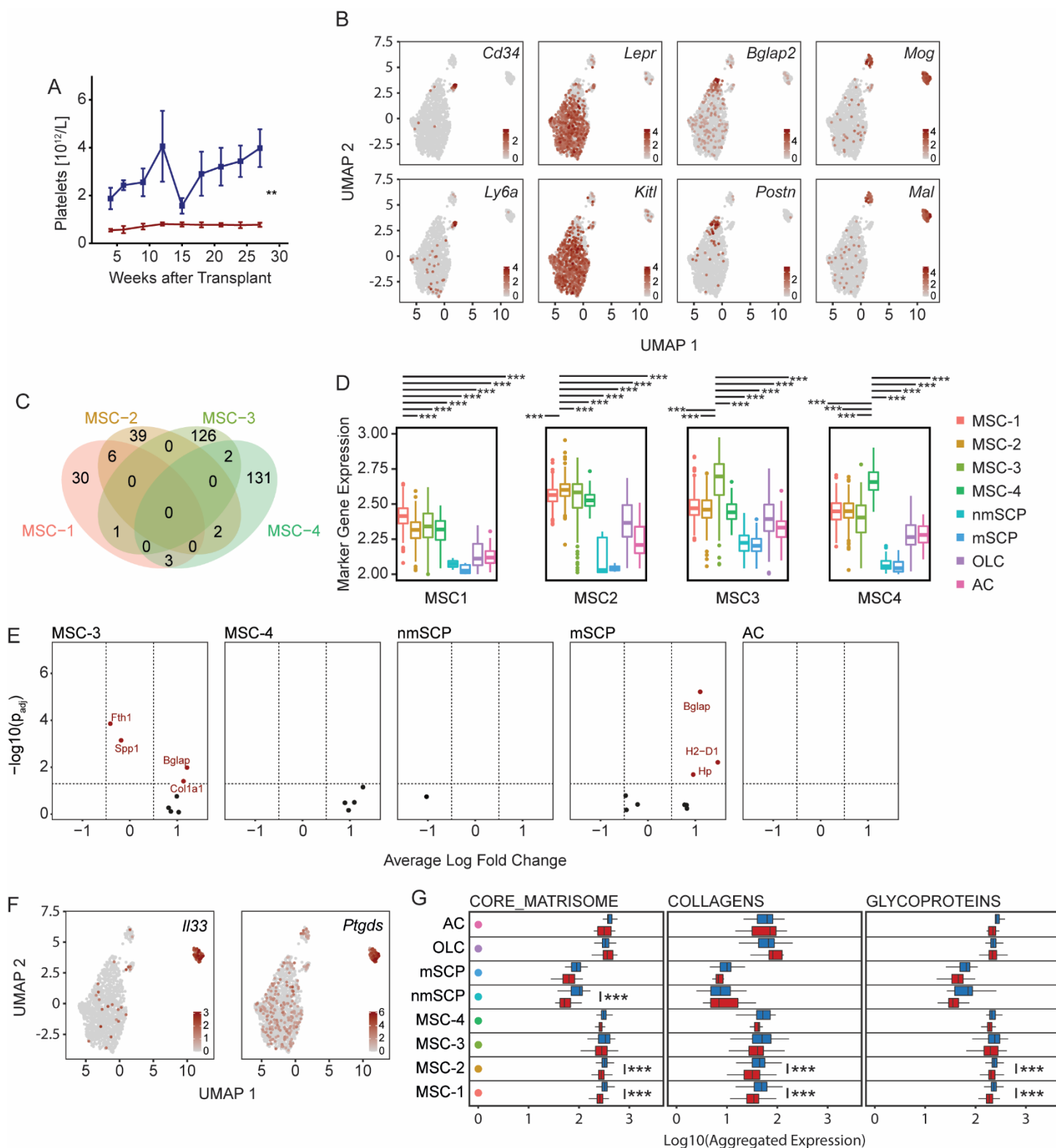


Figure S4: scRNAseq of fibrotic JAK2^{V617F} versus non-fibrotic control mice (related to Figure 4 and Table S2, S3)
(A) Platelet counts over time after transplantation of HSPCs (mean \pm SEM). Significance was determined by Two-Way-Anova with post-hoc pairwise t-test. **(B)** Distribution of selected marker genes in the dataset as shown in Figure 4D is shown in the form of a feature plot as projection of the expression onto UMAP space. **(C)** Venn diagram depicting the count of identified top marker genes of the four identified MSC-populations. Shared markers are highlighted in intersections. **(D)** Boxplot depicting the aggregated gene expression of respective MSC cluster marker genes in each cell population. Significance was calculated by One-Way-Anova and post-hoc pairwise t-test. The interrogated marker geneset was

considered as the respective control for comparisons. p-values were adjusted according to the Benjamini-Hochberg procedure. **(E)** Volcano plot of differentially expressed genes (Wilcoxon Rank Sum Test, two-sided; calculated for each cluster individually) between JAK2^{V617F} and JAK2^{WT} for indicated cell populations. Significantly differentially expressed genes are highlighted in red. **(F)** Boxplot comparing the expression of NABA matrixome associated gene sets in each cluster and comparing the experimental (JAK2^{V617F}; blue) and control (JAK2^{WT}; red) condition. For aggregated gene expression the cumulative gene expression of each geneset per cell was normalized as described. Significance was determined by competitive gene set enrichment analysis. **(G)** Feature plot of *Irf3* and *Ptgds*. Computed expression is projected onto the UMAP space.

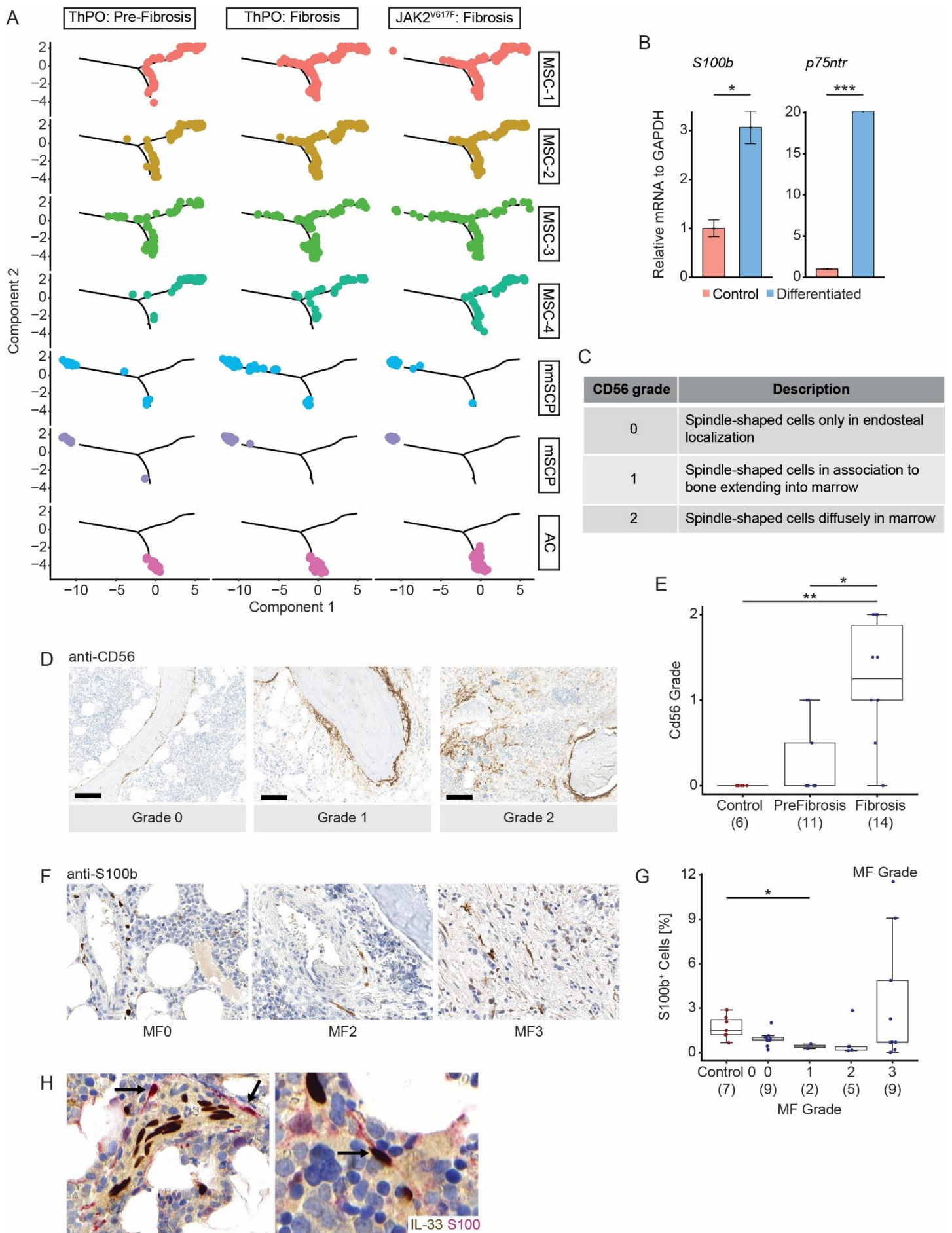


Figure S5: Ligand-Receptor and Pseudotime Analysis of non-hematopoietic clusters in different models of myelofibrosis (related to Figure 5 and Table S6)

(A) Reconstructed cell differentiation trajectory of MSC populations, coloured by cluster identity. Trajectory is shown for every experimental condition (ThPO: Pre-Fibrosis, ThPO:Fibrosis, JAK2V617F: Fibrosis) and each non-hematopoietic cluster individually. **(B)** murine MSCs were isolated and cultured as described before induction of differentiation into Schwann Cell-like cells. Relative mRNA Expression to GAPDH levels was calculated following the $2^{-\Delta\Delta CT}$ -method. Significance was estimated by unpaired t-test. **(C)** Semiquantitative grading of CD56 staining in human bone marrow slides as established on the available cohort. **(D)** Representative images of respective CD56-grades as described in C. Scale bar is set at 100 μ m. **(E)** Comparison of the CD56 grade across different stages of MF. Grading was assessed by two independent researchers. Depicted is the mean of both assessments for each available patient. Significance was estimated by Kruskal-Wallis H test with *post-hoc* Wilcoxon rank sum test. p-values were adjusted for multiple hypothesis testing by the Holm-Bonferroni method. **(F)** Representative images of S100b staining in human bone marrow with varying degrees of bone marrow fibrosis. **(G)** Comparison of the relative frequency of S100+ spindle shaped cells in the bone marrow across different MF grades as shown in (F). Significance was estimated by Welch's ANOVA with *post-hoc* Games-Howell test. **(H)** Immunohistochemical co-staining of IL-33 and S100b showing S100+IL33+ cells (black arrows) in spatial association to arterioles and interspaced between hematopoietic tissue.

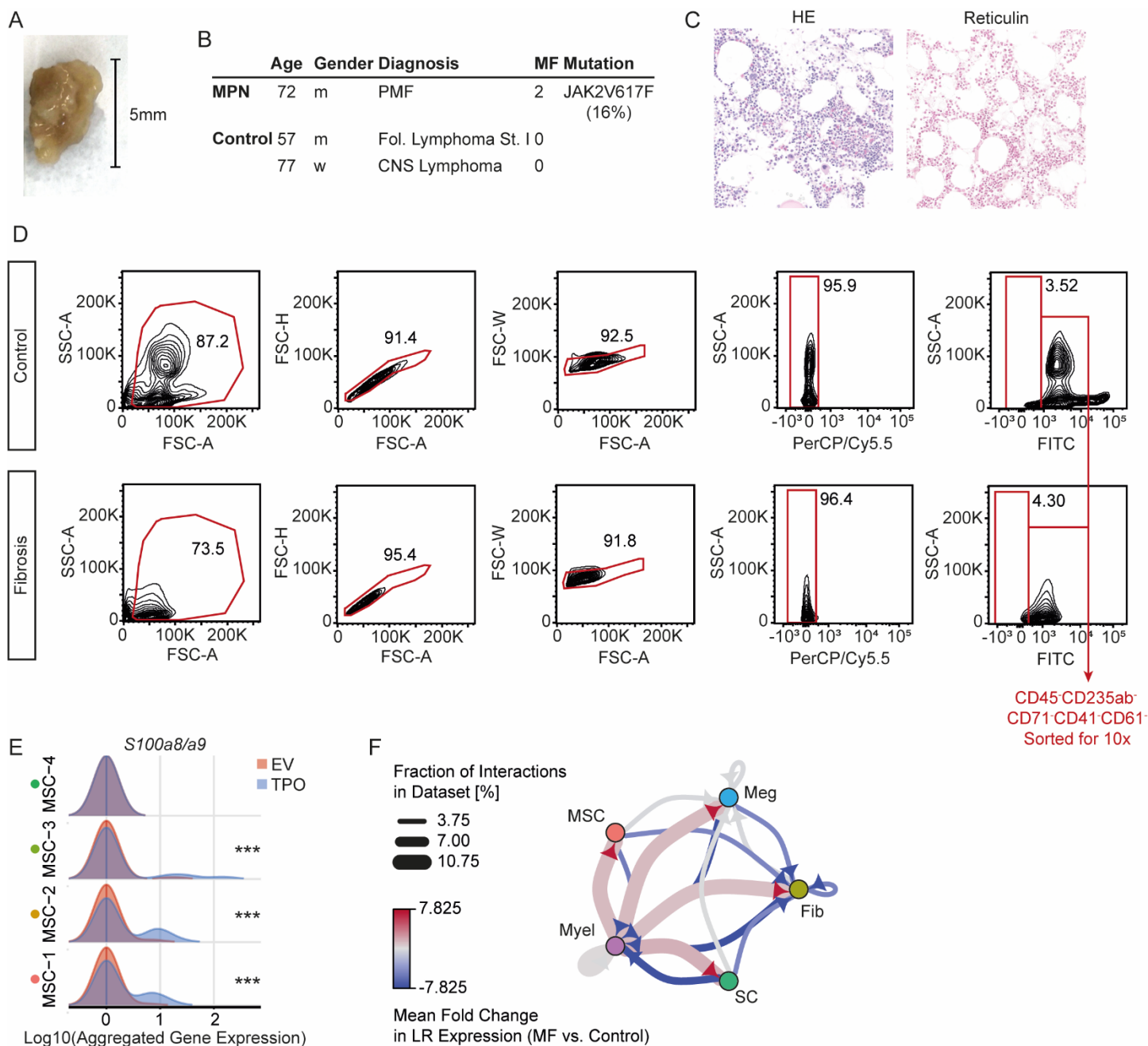


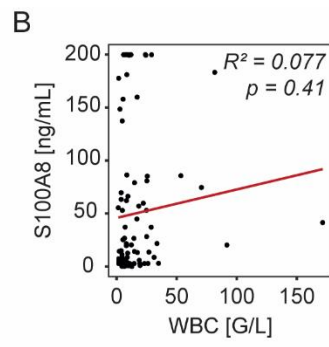
Figure S6: scRNA-sequencing of human fibrotic and non-fibrotic bone marrow shows similar changes in transcription (related to Figure 6 and Table S5)

(A) Representative image of a native bone marrow biopsy used for isolation of non-hematopoietic cells which were subsequently subjected to scRNAseq. **(B)** Clinical information about the patients whose bone marrow was used for single cell transcriptomics. **(C)** Diagnostic HE and reticulin staining of control patient 2. **(D)** Sorting strategy for non-hematopoietic cells. After exclusion of multipllets and non-viable cells, CD45⁻CD235ab⁻CD71⁻CD41⁻CD61⁻ cells were sorted for

scRNAseq. **(E)** Ridgeline plot depicting the expression of *S100a8/a9* in ThPO induced MF (blue) or murine control bone marrow (EV, red). Significance was estimated by modelling the dropout rate as a binomial process with the observed dropout rate per condition as estimator of p for both conditions respectively. **(F)** Network plot showing the mean fold change in S100A8/S100A9 ligand-receptor activity between clusters comparing those derived from fibrotic patient bone marrow to non-fibrotic control bone marrow. Interactions were estimated via CellPhoneDB. Changes in ligand-receptor activity were calculated as the mean of the fold change in ligand expression and in receptor expression comparing fibrotic and control condition. The weight of the edges depicts the number of interactions between two connected nodes divided by the overall number of inferred interactions in the dataset.

A

	MPN	CTRL
n	139	86
age (years)	60.41 (± 1.05)	53.68 (± 3.13)
gender (f/m)	54(38%)/62(44%)	26(29%)/24(27%)
<hr/>		
PMF	69(49%)	
ET	33(23%)	
PV	30(21%)	
MPN-U	7(5%)	
<hr/>		
JAK2V617F	88(63%)	
CALRdel52	24(17%)	
CALRins5	7(5%)	
MPLW515L	6(4%)	
JAK2 Exon 12	1(0,7%)	
Triple Negative	9(6%)	
VAF	50.53% (± 4.69%)	



C

	MPN	CTRL
n	54	9
age (years)	59.10 (± 2.40)	69.11 (± 2.76)
gender (f/m)	22(40%)/17(30%)	4(44%)/5(55%)
<hr/>		
PMF	34(62%)	
ET	7(12%)	
PV	5(9%)	
Other	9(17%)	
<hr/>		
JAK2V617F	34(62%)	
CALRindel	11(20%)	
Triple Negative	3(5%)	
VAF	43.81% (± 8.43%)	

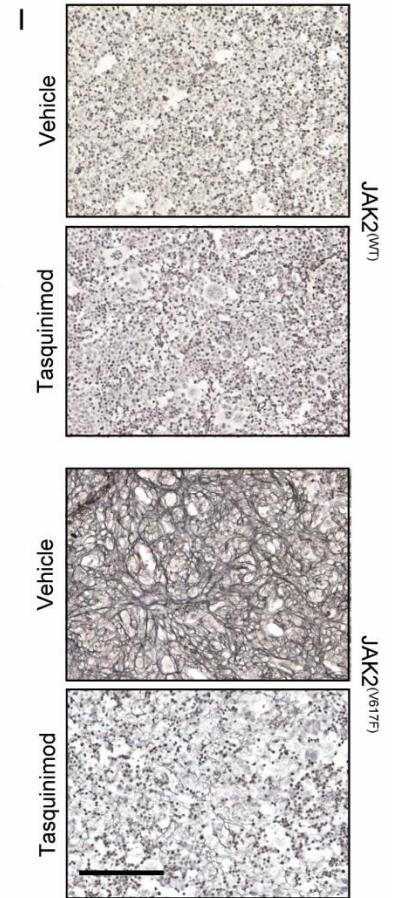
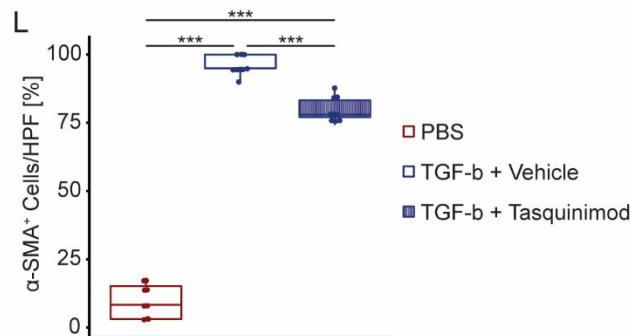
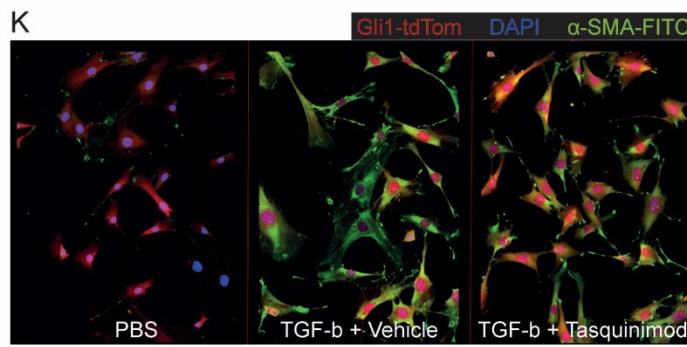
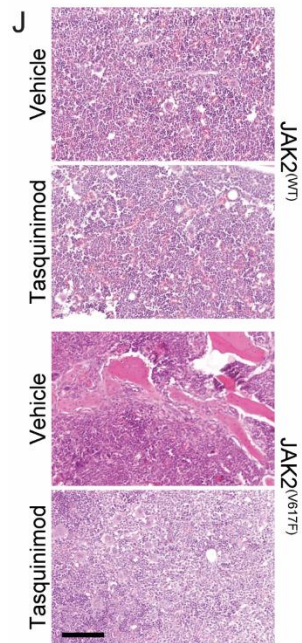
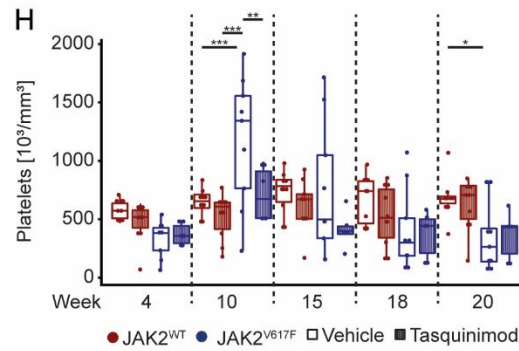
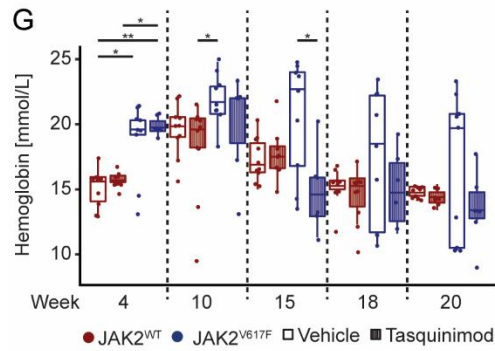
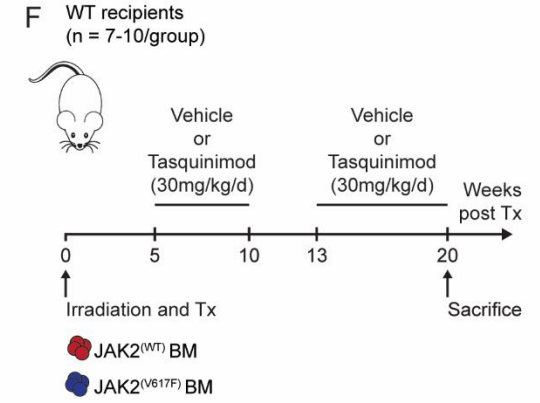
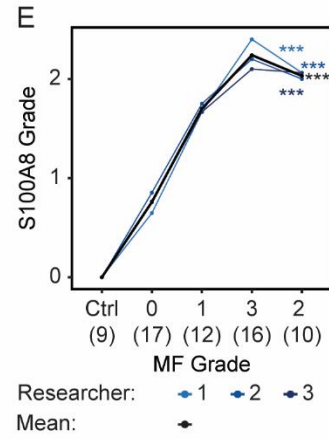
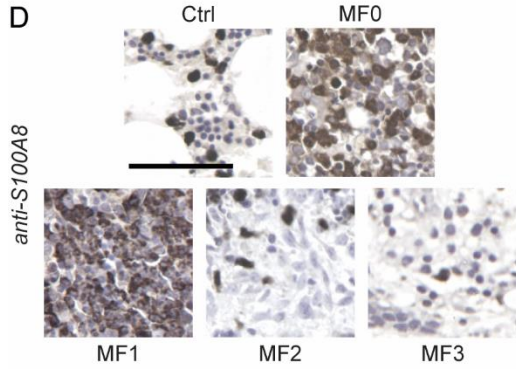


Figure S7: Validation of S100A8 as potential marker of disease progression and therapeutic target in the niche (related to Figure 7)

(A) Patient demographics and disease relevant data of the patient cohort used to measure S100A8 plasma levels. Data is shown as absolute number and relative frequency or as mean \pm SEM. Calculations were performed on all patients, where sufficient clinical data was available. **(B)** Pearson Correlation between the S100A8 Plasma levels as measured by ELISA and the leukocyte count in the peripheral blood. Analysis was performed on all patients, where the corresponding leukocyte count was documented. **(C)** Patient demographics and disease relevant data of the patients whose bone marrow slides were used for S100A8 immunohistochemistry. Data is shown as absolute number and relative frequency or as mean \pm SEM. Calculations were performed on all patients, where sufficient clinical data was available. **(D)** Representative images of S100A8 positivity in the hematopoietic compartment of patient bone marrow. Scale bar: 50 μ m. **(E)** Trend analysis of S100A8 gradings for different MF grades across independent assessments. Depicted is the median grade for each MF grade or control assessed by a single researcher. The mean across all 3 assessments is shown in black as reference. p-values were calculated for each researcher independently and corrected for multiple hypothesis testing by the Benjamini–Hochberg procedure. **(F)** Mice transplanted with JAK2^{V617F}- or JAK2^{WT}-transduced ckit⁺ cells received Tasquinimod (ABR-215050) treatment (30mg/kg/day in drinking water) or vehicle treatment from 5 weeks until 10 weeks, and from 13 until 20 weeks post-transplant. n = 7-10/group. **(G)** Hemoglobin levels and **(H)** Platelet counts of WT mice transplanted with either JAK2^{V617F} (blue) - or JAK2^{WT} overexpressing HSPCs (red) each either treated with Tasquinimod 30mg/kg/day or Vehicle control. A two-way repeated measures ANOVA was performed to evaluate differences between the groups at different timepoints. The effect of the treatment was analyzed at each timepoint. Pairwise comparisons were analyzed by estimated marginal means. **(I)** Representative images of bone marrow reticulin staining in mice transplanted with either JAK2^{V617F}- or JAK2^{WT}-transduced ckit⁺ cells receiving Tasquinimod or vehicle treatment. scale bar: 250 μ m. **(J)** Representative images of HE staining in the bone marrow of control and Tasquinimod-treated mice. scale bar: 100 μ m. **(K)** Mesenchymal stromal cells were isolated and cultured in the presence of either PBS, TGF-b +vehicle control (DMSO) or TGF-b + Tasquinimod for 72h. Cells were stained for α -smooth muscle actin (α -SMA). Representative confocal images for each condition are depicted. **(L)** Quantification of α -SMA⁺ cells per HPF as percentage of total number of cells. Experimental triplicates (n=3) were manually counted by 3 independent researchers. Data is presented as mean \pm SEM. Statistical significance was estimated by One-Way-ANOVA with *post-hoc* Tukey's HSD.

Table S6: Primer List (related to Supplemental Figure S2, S5)

Transcript	Forward	Reverse	Source
Acta2	CTGACAGAGGCACCACTGAA	CATCTCCAGAGTCCAGCACA	
Col1a1	ACGGCTGCACGAGTCAAC	GGCAGGCGGGAGGTCTT	
Cxcl12	CACTCCAAACTGTGCCCTTCA	CACTTTAATTTCCGGTCAATGC	
Gapdh	GGTGAGGCCGGTGCTGAGTATG	GACCCGTTTGGCTCCACCCTTC	
S100b	AACAACGAGCTCTCTCACTTCC	CTCCATCACTTTGTCCACCA	Quintes S et al., 2016
p75ntr	CGGTGTGCGAGGACACTGAGC	TGGGTGCTGGGTGTTGTGACG	Quintes S et al., 2016